ORIGINAL PAPER

Mechanism of aluminium and oxygen ions transport in the barrier layer of porous anodic alumina films

G. Patermarakis · J. Diakonikolaou

Abstract Aluminium was anodised in oxalic acid electrolyte at concentrations 0.125–0.5 M, current densities 25–100 Am^{-2} and low temperatures 0 and 5 °C. The efficiencies of Al consumption and oxide production in the metal| oxide interface and the transport numbers of Al^{3+} and O^{2-} in the barrier layer of porous anodic alumina films were determined. The Al consumption efficiency essentially coincides with that by Faraday's law while that of oxygen evolution, visually detected at these temperatures, is negligible. The oxide production efficiency and O^{2-} transport number decrease with temperature, increase with current density and are almost independent of electrolyte concentration. The transport numbers combined with literature ones for oxalate and sulphuric acid electrolytes were treated by high field kinetic equations describing independent Al^{3+} and O^{2-} transport to penetrate its mechanism. The half jump activation distances were found comparable to ions radii. This mechanism embraces two steps, equilibrium established between ordinary oxide lattice hardly allowing transport and locally emerging transformed structure dispersed in barrier layer consisting of pairs of Al^{3+} and O^{2-} clusters enabling transport and the rate-controlling step of actual ion transport within clusters. The transformed structure then returns to ordinary while it emerges at other sites. The real activation energy of Al^{3+} transport is higher than that of O^{2-}, e.g. by ≈ 19 kJ mol^{-1} at low current densities, but the fraction of really mobile Al^{3+} is $\approx 10^3$–10^4 times larger than that of O^{2-} justifying the not excessively different values of O^{2-} and Al^{3+} transport numbers.

G. Patermarakis (✉) · J. Diakonikolaou
School of Chemical Engineering, Department of Materials Science and Engineering, National Technical University,
Iroon Polytechniou 9, Zografou,
157 80 Athens, Greece
e-mail: gpaterma@central.ntua.gr

Introduction

The science and technology of Al anodising and the mechanism of growth of barrier type and mainly of porous type films has gained a great interest. This is due to that the growth of these films has a high theoretical significance serving as a model for solid-state electrochemical processes and to the exotic self-organised honeycomb porous structure obtained under certain conditions. The barrier type films grow by migration of Al^{3+} outward and O^{2-} inward [1, 2], with respective transport numbers tn_{ca} and tn_{an} ($tn_{ca}+tn_{an}=$ 1). For growth at 100% efficiency, about tn_{ca} portion of film mass is formed at the oxide|electrolyte (o|e) interface by migrating Al^{3+} combined with O^{2-} formed there and the remainder is formed at the metal|oxide (m|o) interface by migrating O^{2-} combined with Al^{3+} formed there. Pores can nucleate and grow only under certain conditions [1]. The growth of porous anodic alumina films (PAAF) occurs when the migrating Al^{3+} are ejected to solution and no film material is added at the o|e interface, thus the efficiency of oxide production at the m|o interface and of film growth coincides with tn_{an}. This was earlier considered roughly around 0.6 [3, 4] but as recently shown [5–8] actually it firmly depends on conditions. Pore filling is prevented by the absence of growth of new oxide at the film surface, while increased stresses from electrostriction assist the stabilisation of pores [3, 4].

The characteristic nanometre scale porous structure, physicochemical properties and strong adherence to Al surface of these films render them suitable for numerous applications. Such applications are the protection, decoration and

upgrading of mechanical properties of Al, rechargeable batteries, magnetic memories, nuclear reactors, fuels cells, templates for synthesising emitters, nanoscience–nanotechnology, catalysis, etc. [9–14]. The pore forming anodising of Al is characterised, e.g. for oxalic, sulphuric and phosphoric acid electrolytes, by a transient stage, where a microscopically flat barrier layer is formed on the surface of which pores are nucleated towards its end [15–19]. This is followed by another transient stage where pores are developed and organised producing the characteristic structure of PAAF [5, 17–27]. The second transient stage is finally followed by the steady-state one. The generation of porous structure thus occurs in the first transient stage [15–19], is integrated in the second one and continues to be reproduced with some probable changes in the steady-state stage.

The steady-state structure of films is characterised as a close-packed array of approximately hexagonal, columnar cells, each of which contains an elongated, roughly cylindrical, pore normal to the surface extending between the film's external surface and the m|o interface, where it is sealed by a thin, compact, hemispherical (or hemispheroid) shell shaped barrier type oxide layer with thickness roughly around 1 nm/V of applied voltage [28–30]. The structure of films is defined by the surface density of pores, usually of the order 10^9–10^{11} cm^{-2}, base diameter of pores, of the order of a few up to several tens of nanometres, shape and ordering degree of pores, which depend on the kind of electrolyte and conditions of Al anodising [29–32]. The oxide, examined after anodising, is an almost anhydrous amorphous (or nanocrystalline) material containing germinal γ or γ'-Al$_2$O$_3$ [29, 30, 33] which is transformed to crystalline γ-Al$_2$O$_3$ by heating at $\approx$700 °C [34]. Hydrogen atoms and electrolyte anions are embodied in small amounts variable across the barrier layer and pore walls depending on electrolyte kind and conditions [18, 29–31, 33]. Anions exist in a pore surface layer leaving an anion almost free layer near the metal and cell boundaries [18, 31].

From the extensive published work on PAAF, a large amount of which is cited in [9, 12], it seems that nowadays the challenging queries are focused mainly on: (i) The mechanism of pores generation and their growth to channel like pores or generally the mechanism of development of porous structure. The main representatives of this mechanism are the thermally and/or field-assisted local dissolution of initially flat film surface [1, 17, 35, 36], the oxygen evolution [37, 38], the oxide material flow [4, 39] and the recrystallisation and oxide densification [40] models; (ii) The attainment of long-range regular porous structure that is crucial for the currently developing technology [20–25, 41]. Perfect hexagonal or other geometry structures on the entire Al surface (perfectly ordered alumina structures) are achieved in a single-step anodising by Al pre-nanoindentation via various techniques [25, 26, 42, 43].

Self-ordered (almost) perfect hexagonal structures in surface domains comparable to 1 μm^2 or to grain surface are achieved by two or more steps anodising at specific conditions after the selective removal of film [25, 41, 44, 45] when anodising is realised within a voltage window specific for each electrolyte. For example this is at $\approx$25 V for sulphuric acid in mild anodising (for hard anodising it is at higher enough voltage) with interpore distance $\approx$63 nm [24, 46], $\approx$40 V for oxalic acid with interpore distance $\approx$100 nm [24, 36, 44] and $\approx$195 V for phosphoric acid with interpore distance $\approx$500 nm [23]. Strictly speaking the self-ordering degree depends heavily on the voltage and to a lesser extent on the rest conditions, like electrolyte concentration and temperature [5, 12]. For galvanostatic anodising best ordering presumably occurs at current densities giving in steady-state voltages vicinal to the above [12, 40, 47]; (iii) The electrochemical (and generally physicochemical) processes taking place at the m|o and o|e interfaces, the ionic transport (and occasionally other processes) across the barrier layer and the determination of related physicochemical parameters. These processes undeniably constitute the core of the entire phenomenon of oxide production and film growth.

Although the relative rates of charge transport by Al^{3+} and O^{2-} in the barrier layer of PAAF, or their transport numbers, can be found by various methods like the determination of oxide production efficiency, implantation of markers etc. [1, 5, 48–50], details on the mechanism of migrations are rather unknown most probably due to the following reasons: (i$_1$) There is no method to follow directly the solid-state ionic transport in the barrier layer during oxide production and film growth in Al specimens immersed in the electrolyte solution capable of giving concurrently proper information. (ii$_1$) The electrochemical kinetic equations tried heretofore to penetrate this mechanism describing rate-controlling processes at interfaces or in thin films like the Cabrera–Mott equation or allied equations describing bulk processes [29, 30, 51] are usually linked with lattice defects generated thermodynamically and/or by field [29, 30, 52] like Frenkel interstitial cations, cations vacancies, etc. However, as above noted these cannot be directly ascertained by some method(s). These equations describe one-step transport and were employed almost solely for one kind ion (cation). For the present the only way to penetrate this mechanism and reveal its details seems to be via combining the ion transport number values with proper kinetic equations not restricted by such a priori admissions and for both Al^{3+} and O^{2-}.

In our earlier works [5, 6, 40], the efficiency of oxide production in PAAF and the Al^{3+} and O^{2-} transport numbers in their barrier layer were determined for oxalic acid and oxalic acid + aluminium oxalate electrolytes at temperatures 10–40 °C and current densities 50–250 Am^{-2} where the demanded anodising voltage was not excessively high as

desired for reasons explained later in subsection Combination of high field equations. Determination of B_2/B_3 and a_2/a_3 of Results and discussion section. Also these were determined for sulphuric acid electrolyte at temperatures 20–35 °C and current densities 50–350 A m^{-2} [7] where uniform/regular film growth could be obtained without appearance of pitting and/or burning phenomena related with non-uniform/abnormal film growth [53]. Along the lines of these works, here the oxide production efficiency and transport numbers are determined during film growth in oxalic acid electrolyte at low enough temperatures 0 and 5 °C and at current densities 25–100 A m^{-2} for which the demanded voltage is not also excessively high. To check any probable participation of oxygen evolution in PAAF growth mechanism, mentioned in the literature [37, 38], its contribution to passing charge was also evaluated. The results derived here together with the above accomplishing each other were further treated by suitably formulated high field electrochemical kinetic equations which embody transport numbers and other physicochemical parameters and describe independent Al^{3+} and O^{2-} transport in the barrier layer of PAAF. By the employed method penetration to the ions transport mechanism has become possible for the first time revealing many important details.

Experimental

Al anodising was performed galvanostatically in vigorously stirred $H_2C_2O_4$ solution at concentrations (c_a) = 0.125, 0.25 and 0.5 M, temperatures (T) = 0 and 5 (± 0.1–0.2) °C, current density (j) = 25, 50 and 100 A m^{-2} and times (t) up to 5,400 s. The j's employed are relatively low to assure that the demanded voltage for all t's is not high enough to avoid high rate of heat evolution in the anode that would cause a notable rise in the real anodising T (temperature in the barrier layer region), enlarged with rising j and falling T [32], thus differing notably from the T of bulk solution and degrading the reliability of results. The maximum t employed, 5,400 s, was longer enough than that at which the steady state has been first established and shorter than that at which the maximum limiting thickness is first established where all neighbouring pore mouths are interconnected in surface due to the enlargement of pores to film surface resulting from the attack of pore walls by the aggressive electrolyte [29, 30, 32]. This is also smaller than excessively long t's beyond which the porous structure at the external film layer is collapsed which is also attributed to this attack [54]. Two face Al sheets anodic electrodes 5× 5 cm with thickness 0.3 mm and purity ≥99.95% (Merck— pro analysi) with total geometrical surface to be anodised (S_g)=50.95 cm^2 and two Ti cathodic electrodes of similar geometry were used. This relatively large surface was used

to minimise the relative errors of determination of consumed Al and product oxide masses. The determination of the accurate masses of consumed Al and product oxide are essential for the accuracy of ensuing analysis.

Prior to anodising the Al specimens were degreased, etched chemically by chromophosphoric acid solution, which removes the oxide (either natural or anodic) and leaves intact the Al substrate [29, 30, 32], washed by distilled water and dried in air stream. After anodising, carried out as described in detail elsewhere [32], the specimens were washed by distilled water, immersed in distilled water and neutralised with NaOH 0.1 M in drops using as indicator bromo-thymol blue (pH range 6–7.6). This was done to remove the electrolyte probably remaining in the narrow pores. Finally, they were washed, dried in air stream and remained in a desiccator for at least 24 h. The enclosure of acid in pores after drying in air stream of non-neutralised anodised specimens disturbs the actual oxide mass value and results in the inclusion of additional amount of electrolyte species in barrier layer and pore wall oxide [55]. Neutralised and desiccated oxide is almost anhydrous with contained H_2O<0.5% [32], while the amount of contained oxalate anions, 2–3% [1, 12, 31], must be even lower in neutralised films. Thus in the formed films the contained electrolyte anions are not taken into account.

The mass of Al consumed during anodising was found from the difference of Al masses (weighed with sensitivity 10^{-5} g) prior to anodising and after anodising and selective removal of oxide by the above solution at 60–70 °C. This mass was compared with that predicted by Faraday's law. The mass of oxide formed on Al was found with this sensitivity by two methods for comparison purposes: (i$_2$) By the difference of the mass of anodised Al specimen (neutralised and desiccated as above) and the mass of Al metal after the selective removal of oxide, washing and drying; (ii$_2$) By a suitable mass balance method from the initial mass of Al specimen and the final after anodising, washing, neutralisation and desiccation. The above comparisons and suitable treatment of consumed Al and formed oxide masses at various conditions can offer much detailed information for Al oxidation, film growth mechanism and related parameters. The oxide mass, experimentally determined with high accuracy, depends on electrolyte kind, anodising conditions and time via the film growth mechanism embracing electrochemical processes in barrier layer and interfaces and chemical oxide dissolution of pore walls and film surface. Suitable kinetic models are formulated, embracing proper structural and kinetic parameters, describing the dependence of oxide film mass on time and conditions. Their application, taking into account the film mass at various times and conditions, can yield values for many structural and kinetic parameters related with film growth mechanism [5–7, 40, 55]. The charge consumed from

oxygen evolution on Al anode, visually detected at the employed low T's, was also thus estimated. The oxide mass values were also used to determine the efficiency of film growth and transport numbers of Al^{3+} and O^{2-} in the barrier layer during film growth. These results together with earlier ones for electrolytes $H_2C_2O_4$ 0.5, 1.0 and 1.5 M and $H_2C_2O_4$ (0.5 M) + $Al_2(C_2O_4)_3$ (0.1, 0.25 and 0.5 M) at $T=$ 10, 15, 20, 25, 30, 35 and 40 °C and $j=$50, 150 and 250 A m^{-2} [5, 6, 40] and H_2SO_4 1.53 M at $T=$20, 25, 30 and 35 °C and $j=$50, 150, 250 and 350 A m^{-2} [7] were also used in the ensuing analysis.

Al anodising was followed chronopotentiometrically. The anodic potential (vs. usual reference electrodes) approximately represents the potential drop from the m|o to the o|e interface [56, 57]. The anodic potential (vs. Ag/AgCl reference electrode attached laterally and closely to Al electrode) and anodising voltage were both followed. This voltage was higher than anodic potential by ≈1.2, 1.1, 1.2, 1.3, 1.9 and 2.6 V, respectively for the employed conditions (c_a, T, j), (0.5 M, 0 °C, 50 A m^{-2}), (0.5 M, 5 °C, 50 A m^{-2}), (0.25 M, 0 °C, 50 A m^{-2}), (0.125 M, 0 °C, 25 A m^{-2}), (0.125 M, 0 °C, 50 A m^{-2}) and (0.125 M, 0 °C, 100 A m^{-2}). Chronopotentiometric curves are used among others to define the three stages of PAAF growth.

Results and discussion

Chronopotentiometric study and PAAF growth stages

The plots of anodic potential (P_{an} vs. Ag/AgCl) vs. t up to the maximum t employed appear in Fig. 1a while Fig. 1b presents a magnification of plots at low t's. Figure 1 provides the next already noted successive stages and substages defined by points A, B and C corresponding to times t_A, t_B and t_C. The first stage is 0B characterised by abrupt rise of P_{an} with t that is initially almost linear but is gradually retarded so that the P_{an} vs. t plot declines to the right mainly to the end of stage at t_B. It embraces the transient substage 0A with duration about 2/3 that of 0B in which a microscopically flat barrier layer is developed and the substage AB where the nuclei of porous structure are generated [15–19]. The duration of stage 0B about 40–160 s in the employed conditions decreases with T, j and c_a. The final maximum P_{an} value rises with rising j and falling c_a and T. The subsequent stage is BC where P_{an} drops up to t_C roughly about 10 min. In this stage the nuclei are transformed to pockets and then to channel like pores. Also, the pore/cell system units further develop and cover gradually all the surface and are self-organised within domains comparable e.g. to metal grain surfaces towards the Al substrate side. The attained order of cells/pores varies from regular almost perfect hexagonal at specific anodising conditions [5,
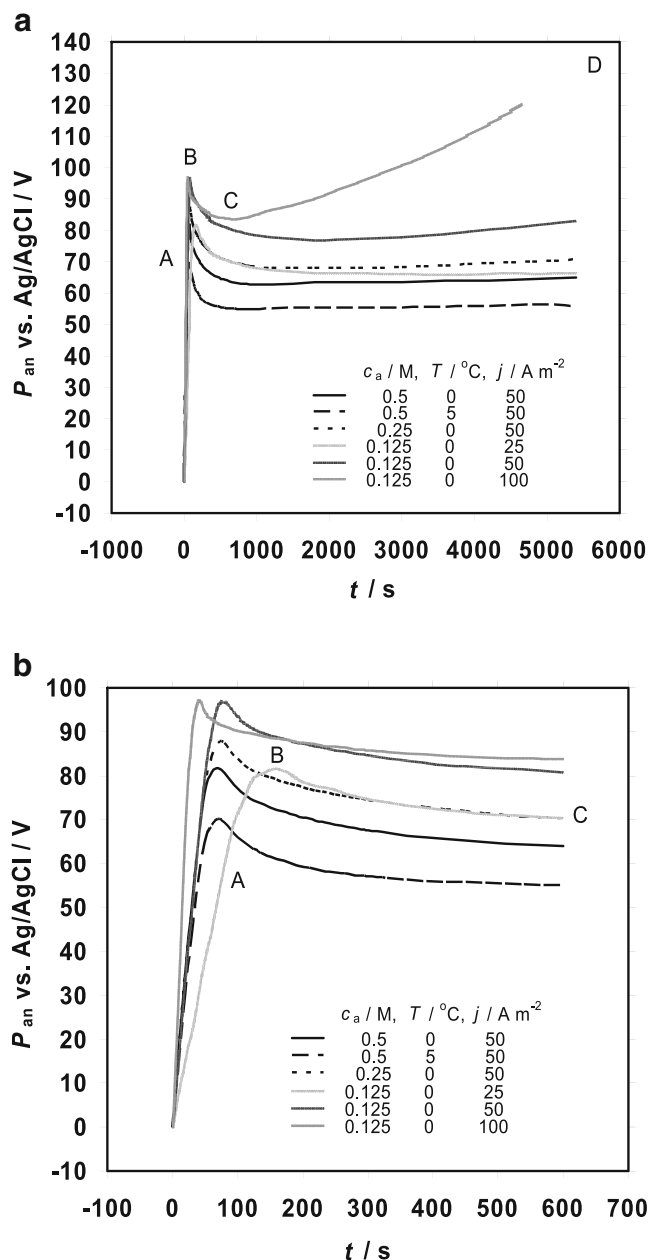
Fig. 1 **a** Plots of anodic potential vs. time, P_{an} (vs. Ag/AgCl) vs. t, during Al anodising in $H_2C_2O_4$ solution at current densities $j=$25, 50 and 100 A m^{-2}, temperatures $T=$0 and 5 °C and $H_2C_2O_4$ electrolyte concentrations $c_a=$0.125, 0.25 and 0.5 M up to the longer time t employed. **b** Magnification of plots in the region of short t's

20–27] up to poorer enough at other conditions. Its duration drops with j, c_a and T while the dependence of the final P_{an} on T, j and c_a is similar to that of peak P_{an} at t_B. The final stage CD is the steady-state stage where P_{an} rises slightly with t at higher c_a's and T's and lower j's and strongly at the lowest c_a and T and higher j. The almost final cellular columnar porous structure to the Al side has been already established in the start of this stage [5, 19]. Then this structure is steadily reproduced with some changes [47,

55]. Since the anodic potential is variable during the stage CD, and this is valid also for structural features [47, 55], this is actually a quasi-steady state. The plots in Fig. 1 are typical for Al anodising in pore-forming electrolytes but the characteristic t's and P_{an}'s depend strongly on electrolyte kind, T and j. At corresponding conditions as a rule these decrease in the order phosphoric, oxalic and sulphuric acid.

The potential drop in pores is negligible compared to P_{an} [29, 56]. Thus P_{an} essentially represents the potential drop from Al to pore base electrolyte. During Al anodising this potential drop and occurring processes are divided into those in the barrier layer oxide and in the m|o and o|e interfaces. For sufficiently thick flat barrier layer formed during the substage 0A, e.g. for $t \geq 1$ s at the employed j's, or for the flat layer carrying insipient pores (nuclei) in substage AB, or for the scalloped one in stages BC and CD the potential drops in interfaces are tiny compared to that in oxide [57, 58]. Thus P_{an} basically represents the potential drop inside the barrier layer. For such sufficiently thick films the rate-controlling processes are those inside the film and not in interfaces [57, 58]. This is strongly supported by the fact that for a given electrolyte the potential drop across the barrier layer (varying with conditions) increases almost linearly with barrier layer thickness by $\approx$ 1 V nm^{-1} [28–30]; if the rate-controlling step was the charge transport or other process at interface(s) this would not occur.

Determination of the electrochemical efficiencies for Al oxidation and oxide production in the m|o interface and of O^{2-} and Al^{3+} transport numbers

The examination of Al metal consumption during anodising has a specific significance for low T's where oxygen evolution was visually detected. The Al consumption by electrochemical oxidation, Al$-3e^- \rightarrow$Al^{3+}, found by selective oxide dissolution ($m_{Al,sod}$) essentially coincides with that anticipated by Faraday's law ($m_{Al,F}$), Fig. 2. By regression analysis the gradients and intercepts of linear plots were determined that are given in Table 1. The intercept is always of the order of mass determination sensitivity 10^{-5} g either positive or negative but its average value is approximately -1.4×10^{-5} g and expresses on average the attack of Al substrate by the solution of selective oxide removal that is negligible. The value of 100×(gradient by Fadaray's law −experimental gradient)/(gradient by Fadaray's law) is 0.13%, 0.14%, 0.28%, −0.01%, 0.14% and 0.13%, respectively for the conditions 1–6 in Table 1. The tiny positive deviation of inclinations (except one case where it is negative but close to zero) predicts negligible rate of charge consumption by oxygen evolution. Thus even at the low T's and rest conditions used the electrochemical efficiency for Al consumption is close to 100%. The ionic current in
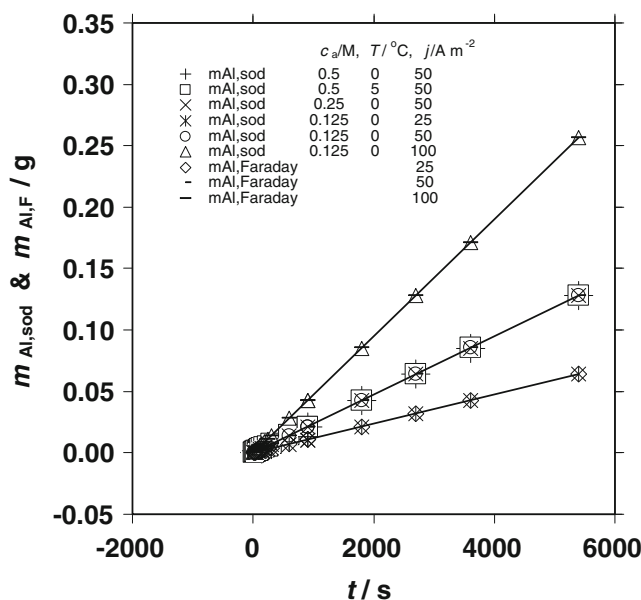

Fig. 2 Dependence of consumed Al mass during anodising on time t at current densities j=25, 50 and 100 A m^{-2}, temperatures T=0 and 5 °C and H$_2$C$_2$O$_4$ electrolyte concentrations c_a=0.125, 0.25 and 0.5 M. The linear plots of consumed Al mass predicted by Faraday's law are given for comparison

the m|o interface from the Al side due to Al oxidation or that corresponding to Al^{3+} entering the oxide bulk is thus faradaic.

For assisting comprehension of the following the processes in the barrier layer either flat or hemispherical in steady state, Fig. 3, in pore-forming electrolyte [5] are shown in Table 2 consistent with faradaic Al consumption verified also for oxalate electrolytes at higher T's and various other conditions [6, 40] as well as for H$_2$SO$_4$ at various conditions [55]. An amount of Al^{3+} ions thus formed in the m|o is combined with migrating O^{2-} ions [48] reaching this interface to form oxide while the rest amount migrates through the oxide bulk and is finally ejected to solution [48, 59] and complexed with water [60, 61]. Quantitatively all migrating Al^{3+} in the barrier layer when reaching the o|e interface are ejected; also quantitatively all O^{2-} migrating inside the barrier layer reaching the o|e interface come from water decomposition. The surface of oxide at pore bases is continuously reformed and deformed on moving to the Al side in unison with e.g. the scalloped barrier layer in agreement to plastic flow [4, 39] and oxide recrystallisation and densification to surface [40] models of PAAF growth and to the experimentally verified shift of surface O^{2-} [62] to Al side. Because the surface anions and cations are shifted together, their movement does not create net ionic current. Ionic current is produced only by the counter migrating anions and cations. In the above processes the migrating ions and the ions in lattice sites (whatever can be meant as lattice for this amorphous material) or in surface

Table 1 Gradients and intercepts of the linear plots mass of consumed Al found by selective oxide dissolution vs. anodising time in Fig. 2 at various conditions (1–6), concentration of $H_2C_2O_4$ c_a, temperature T and current density j

Condition number	c_a/M	T/°C	j/A m^{-2}	$10^5 \times$gradient/g s^{-1}	$10^5 \times$intercept/g	$10^5 \times$gradient by Faraday's law/g s^{-1}	tn_{an} (0B)	tn_{an} (CD)
1	0.5	0	50	2.37149	−5.8	2.37460	0.791	0.786
2	0.5	5	50	2.37139	2.7	2.37460	0.765	0.757
3	0.25	0	50	2.36794	5.1	2.37460	0.819	0.792
4	0.125	0	25	1.18741	−4.5	1.18730	0.724	0.750
5	0.125	0	50	2.37427	−4.6	2.37460	0.779	0.781
6	0.125	0	100	4.74335	−1.4	4.74967	0.879	0.798

Correlation coefficients were always practically 1. For comparison the gradients predicted by Faraday's law are given. The O^{2-} transport numbers tn_{an} in the first transient and steady-state stages are also cited

sites of flowing material can mutually change during film growth but the net ionic current result is that described above.

The ionic current in the m|o interface has to coincide with that at each position across the barrier layer. The migrating ions are almost exclusively O^{2-} and Al^{3+} in the region adjacent to this interface where nearly pure oxide exists. In the o|e interface H_2O is decomposed to H^+ ejected to solution and O^{2-} migrating to the m|o interface and/or H_2O is dissociatively adsorbed on Al^{3+} and O^{2-} surface sites producing OH^- the major part of which is decomposed to O^{2-} and H^+ moving as above and the rest enters the oxide bulk [12, 56]. In the region of barrier layer contaminated by electrolyte anions and OH^- the migrating anions are mainly O^{2-} and secondarily OH^- and electrolyte anions while cations are mainly Al^{3+} and secondarily H^+ [5, 18, 29–31, 33]. The minor OH^-, electrolyte anions and H^+ contributions to ionic current are located mainly near the o|e interface and drop rapidly to the m|o interface direction. Thus as a whole the central role in the processes in barrier layer is played by the transport of Al^{3+} and O^{2-} ions across it during oxide production and film growth. From the above it is apparent that the ionic current across the barrier layer is practically close to 100% of imposed current while the electronic

Fig. 3 Schematic representation of hemispherical barrier layer of porous anodic alumina films in steady state; the pore base diameter, D_b, the cell width, D_c, and a section surface S across the barrier layer corresponding to diameter D are shown

current, related to galvanoluminescence during anodising [63] and to oxygen evolution, is tiny even at T's as low as 0 and 5 °C. The electronic current allied with oxygen evolution, lying as shown in the region of zero, under high field action most probably occurs via tunnelling effect; thus it must not violate the ions transport mechanism and related electrochemical kinetic equations.

The mass balance equation that gives oxide mass ($m_{ox,mb}$) and embraces faradaic Al consumption is thus

$$m_{ox,mb} = \Delta m + m_{Al,F} = \Delta m + j S_g t (AM_{Al})(3F)^{-1}, \quad (1)$$

where Δm is the difference of masses of Al specimen after and prior to anodising, $m_{Al,F}$ is consumed faradaic Al mass, AM_{Al} is the atomic mass of Al and F is Faraday's constant (96,487 $C\,mol^{-1}$). The $m_{ox,mb}$ and the oxide mass found by the selective oxide dissolution ($m_{ox,sod}$) essentially always coincide, Fig. 4, verifying the accuracy of Eq. 1. Obviously, the $m_{ox,mb}$ or $m_{ox,sod}$ found is non-faradaic. The oxide mass decreases imperceptibly with T. Smooth curves rising with t are observed at all conditions without any breaking points or other characteristic features e.g. in the boundaries of successive transient (sub)stages 0A, AB and BC. This result confirms that the generation and evolution of pores is not associated with some preferable locally accelerated detectable oxide consumption beyond t_A or t_B, Fig. 1, due e.g. to some kind of local oxide dissolution, either chemical or electrochemical. In other words the mechanism of pores nucleation and growth does not involve any field-assisted dissolution of oxide [35]. If it were true, a considerable gradual reduction of the rate of oxide production by a percentage varying from 0% around A up to a value higher than porosity of PAAF near barrier layer established at point C would be observed, which is not the case. The final retardation of oxide production around C should be larger than this porosity since the oxide density at the pore base surface is higher than the average across the barrier layer [6]. The porosity near barrier layer is roughly 0.10–0.19 and above [6, 23] depending on conditions. This retardation is negligibly affected by the much slower purely chemical
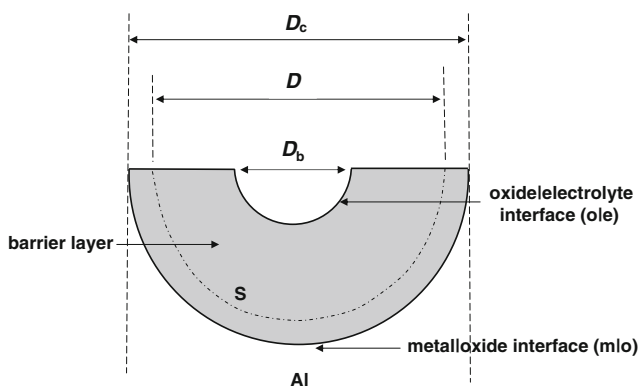
Table 2 Processes taking place at the metal|oxide and oxide|electrolyte interfaces and in the pure and contaminated oxide sublayers of barrier layer (either flat or scalloped) during film growth in pore forming electrolyte; tn_{ca} and tn_{an} are transport numbers of Al^{3+}, tn_{an}', $tn_{electrolyte\ anions}$, tn_{OH^-} and tn_{H^+} are transport numbers in contaminated sublayer of O^{2-} and of species noted in indices

Processes at the metal|oxide interface	Processes in pure oxide sublayer	Processes in contaminated oxide sublayer	Processes at the oxide|electrolyte interface
1. Al oxidation obeying Faraday's law $Al-3e^- \rightarrow Al^{3+}$	Ionic current is due to migration of Al^{3+} (tn_{ca}) and O^{2-} (tn_{an}), $Al^{3+} \rightarrow (tn_{ca} < 1)$, $\leftarrow O^{2-}(tn_{an} < 1)$, $tn_{ca} + tn_{ca} = 1$ (electronic current is close to zero, or passing current is closely totally ionic)	Ionic current is due to migration of Al^{3+} (tn_{ca}), O^{2-} (tn_{an}'), electrolyte anions ($tn_{electrolyte\ anions}$), OH^- (tn_{OH^-}) and H^+ (produced from OH^- decomposition, $OH^- \rightarrow O^{2-} + H^+$) ($tn_{H^+}$) $tn_{an} = tn_{an}' + tn_{electrolyte\ anions} + tn_{OH^-} + tn_{H^+}$, ($tn_{electrolyte\ anions} + tn_{OH^-} + tn_{H^+} << tn_{an}'$)	1. Ejection of Al^{3+} to electrolyte
2. Entrance of product Al^{3+} in the oxide space adjacent to interface			2. H_2O decomposition producing H^+ ejected to solution and O^{2-} migrating towards the metal|oxide interface and/or H_2O dissociative adsorption on Al^{3+} and O^{2-} surface sites producing OH^- a portion of which enter the oxide bulk
3. Combination of tn_{an} portion of formed Al^{3+} with migrating O^{2-} arriving at the metal|oxide interface to form oxide, $2Al^{3+} + 3O^{2-} \rightarrow Al_2O_3$ 4. Migration of the rest Al^{3+} at portion tn_{ca} towards the oxide|electrolyte interface		Contribution of electrolyte anions, OH^- and H^+ is minor occurring mainly near oxide|electrolyte interface. It falls rapidly towards the metal|oxide interface. Near boundary with pure oxide sublayer it becomes zero ($tn_{an}' = tn_{an}$)	3. Incorporation of electrolyte anions

dissolution by the electrolyte of the external film surface and wall surface of nuclei/pockets/pores; this rate is e.g. for H_2SO_4 15% w/v (1.53 M) electrolyte 0.04–0.12 nm min^{-1} at $T=20$–30 °C [55] and considering the much lesser aggressive ability of $H_2C_2O_4$ this rate is estimated $<<$ 0.01 nm min^{-1} for $H_2C_2O_4$. Instead the generation and evolution of pores is consistent with the plastic flow [4, 39] and recrystallisation and oxide densification [40] models.
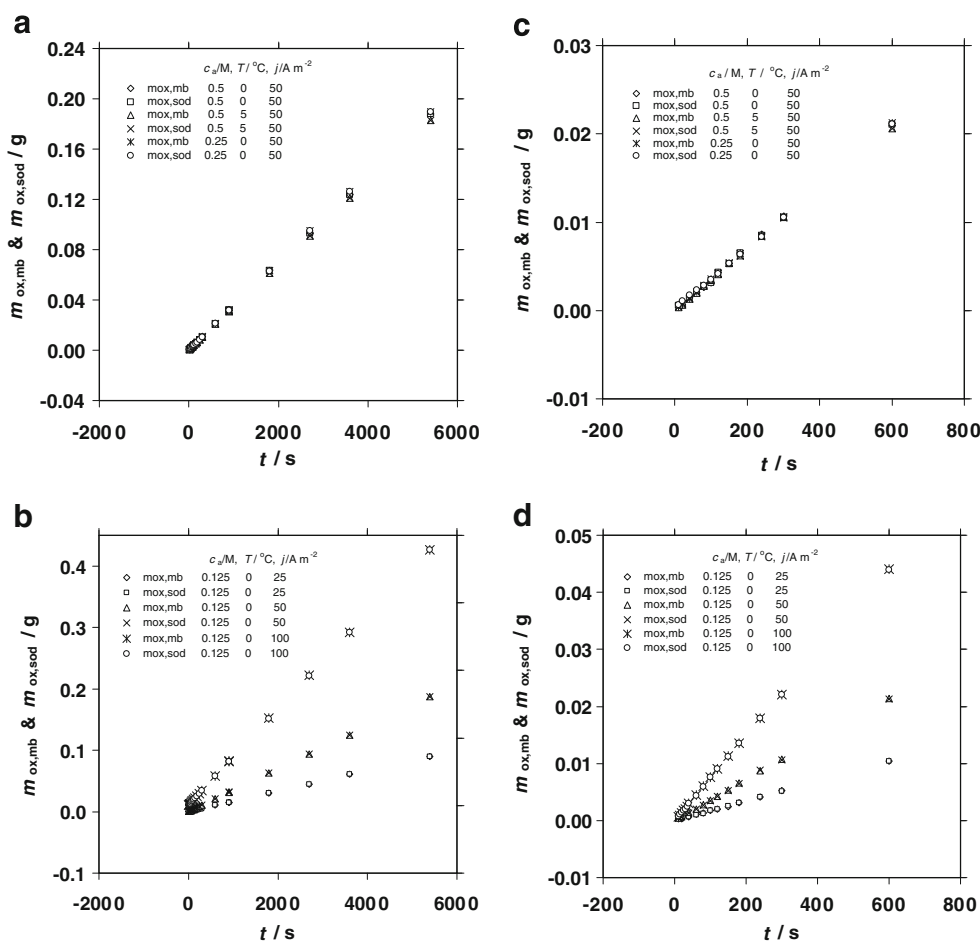
During film growth in pore-forming electrolytes the oxide is produced exclusively in the m|o interface at a rate $kS_g jtn_{an}$, where $k=MM_{Al2O3}(6F)^{-1}=1.761\times10^{-4}$ g C^{-1}, MM_{Al2O3} is the molar mass of Al_2O_3 and tn_{an} is both the electrochemical efficiency for oxide production at this interface and O^{2-} transport number. During the first transient stage 0B the tn_{an} is thus determined by equating $kS_g jtn_{an}$ with the gradient of $m_{ox,mb}$ vs. t plots, Fig. 4, for $t \leq t_B$, Fig. 1. Their values are given in Table 1. The electrochemical efficiency for oxide production and tn_{an} in steady state are found by the method outlined elsewhere [5]. The plots of dimensionless factor $(\Delta m_{ox,mb}/\Delta t)(kjS_g)^{-1}$ vs. Δt, Fig. 5, must obey the Eq. [5]

$$(\Delta m_{ox,mb}/\Delta t)(kjS_g)^{-1} = tn_{an} + z_1(\Delta t)$$
$$+ z_2(\Delta t)^2, (z_1 \text{ and } z_2 < 0) \qquad (2)$$

where $\Delta t = t - t_C > 0$, $\Delta m = m_{ox,mb}(t) - m_{ox,mb}(t_C)$, t_C here is around 600 s and z_1, z_2 are factors depending on all anodising conditions and electrolyte kind and composition which incorporate also the attack of pore walls by the electrolyte; for small enough rate of oxide dissolution $z_2 \approx 0$. The above equation determining tn_{an} is based on the mechanisms of oxide production and film growth and takes into account the characteristic porous film structure in steady state. The small negative inclination of plots in Fig. 5 shows that the rate of pore wall dissolution is small, but even at such low T's as 0 and 5 °C the pore wall oxide dissolution still persists to be detectable. The tn_{an} values thus found are given in Table 1. The corresponding transport numbers of Al^{3+} are $tn_{ca} = 1 - tn_{an}$. Instead $m_{ox,mb}$ the $m_{ox,sod}$ could be used giving closely identical results; the $m_{ox,mb}$ was chosen as its determination anticipates fewer experimental step measurements and thus smaller experimental errors are expected.

Table 1 shows that tn_{an} of both stages increase with falling T and rising j. Some fluctuation of their values is observed with the change of c_a. Since their mean values at $j=50$ Am^{-2}, $T=0$ °C and $c_a=0.125$, 0.25 and 0.5 M for stages 0B and CD respectively 0.796 and 0.786 are very close to those at $c_a=0.5$ M, then c_a seems not exerting any significant effect on tn_{an} in both stages. At lower j's a trend for a slight decrease of tn_{an} from 0B to CD stage is observed for the most of conditions (transgressed in fewer ones) which

is explained by that the real surface of ionic current passage in the m|o interface and on average across the barrier layer is larger in steady state and thus the real current density decreases causing some slight drop of tn_{an}. Another reason
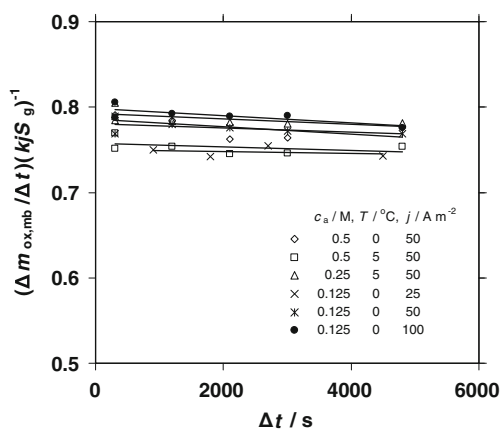

Fig. 5 Plots of dimensionless factor $(\Delta m_{ox,mb}/\Delta t)(kjS_g)^{-1}$ vs. Δt in steady-state stage at current densities j=25, 50 and 100 A m^{-2}, temperatures T=0 and 5 °C and electrolyte concentrations c_a=0.125, 0.25 and 0.5 M

must be that as film thickens the heat produced in the barrier layer region is less easily dissipated to bath solution resulting in a rise of real anodising temperature and thus to some decrease of tn_{an}. Thus when comparing the P_{an} vs. t plots for c_a=0.125 M and j=50 and 100 Am^{-2}, Fig. 1, though the second j is twice the first, the anodic potentials at t's from about t_B up to about t_C do not differ significantly. This is well explained by the rise of real anodising temperature the difference of which from the imposed T becomes notable mainly at high j's and low T's; this in turn causes a lower increase of required potential than that if the real anodising temperature were stable and equal to T. The two reasons cooperate. The second reason must become more significant as j rises justifying the notable decline of tn_{an} from 0B to CD at j=100 A m^{-2} consistent with the on average higher enough P_{an} and its tendency to rise strongly in steady state. Thus treatment of results at high j's and low T's for oxalate electrolytes to estimate physicochemical parameters considering that the anodising temperature equals T must include some inherent errors and at low T's this must be limited to low j's. That is why j's≤100 Am^{-2} were applied here. The trends of tn_{an} variation with conditions agree with those at higher T's [5–7, 40] allowing their treatment together.

High field ionic transport equations

The geometry of barrier layer in steady stage is stable in the case of unaltered structure around the barrier layer i.e. at conditions of best ordering and for relatively short t's or low film thicknesses. For prolonged anodising at conditions of best ordering [47] as well as at conditions other than those [55] the surface density of cells/pores gradually decreases and the average cell width, pore base diameter and thickness of barrier layer increase with a parallel slight rise of P_{an} [47, 55]. But despite this, the surface area of m|o interface, film porosity in the barrier layer region and the surface area of o|e interface remain closely constant [55]. Thus without injuring the reality it can be considered that the slow change of structure (consistent with not strong/abrupt rise of P_{an} in steady state) does not affect the ensuing analysis which describes the ions transport in either ordered or non-ordered films. Irrespective of details of the actual ion transport mechanism the real O^{2-} and Al^{3+} partial ionic current densities through an equipotential surface S across the hemispherical barrier layer, Fig. 3, characterised by identical electric potential at each its point that varies however across this layer [6], with area S in steady state $j_{t,an} = jtn_{an}S_gS^{-1}$ and $j_{t,ca} = jtn_{ca}S_gS^{-1}$ must obey the high field strength (of the order ≈ 1 V nm^{-1} [28–30]) equations [5, 6]

$$jtn_{an}S_gS^{-1} = N_{2,m}\nu_2 n_2 F N_A^{-1} \exp[(-W_2' + n_2 a_2 FE)/(RT)] \tag{3a}$$

$$jtn_{ca}S_gS^{-1} = N_{3,m}\nu_3 n_3 F N_A^{-1} \exp[(-W_3' + n_3 a_3 FE)/(RT)] \tag{3b}$$

or

$$\begin{aligned} \ln(jtn_{an}) &= \ln\left[\left(S/S_g\right)\left(N_{2,m}\nu_2 n_2 F N_A^{-1}\right)\right] \\ &\quad + (-W_2' + n_2 a_2 FE)/(RT) \\ &= \ln A_2 + (-W_2' + B_2 FE)/(RT) \end{aligned} \tag{4a}$$

$$\begin{aligned} \ln(jtn_{ca}) &= \ln\left[\left(S/S_g\right)\left(N_{3,m}\nu_3 n_3 F N_A^{-1}\right)\right] \\ &\quad + (-W_3' + n_3 a_3 FE)/(RT) \\ &= \ln A_3 + (-W_3' + B_3 FE)/(RT), \end{aligned} \tag{4b}$$

where $N_{2,m}$ and $N_{3,m}$ are the surface concentrations of mobile O^{2-} and Al^{3+} ions in each equipotential surface across the barrier layer (m^{-2}), ν_2 and ν_3 are the vibration frequencies of O^{2-} and Al^{3+} ions or the number of chances per second the ions may jump the energy barrier (activation energy) if they have sufficient energy (s^{-1}), n_2 and n_3 are the valences of O^{2-} and Al^{3+}, N_A is Avogadro constant

$(6.022 \times 10^{23}$ mol$^{-1})$, W_2' and W_3' are the activation energies of O^{2-} and Al^{3+} transport in oxide (>0; J mol^{-1}), a_2 and a_3 are the activation (half jump) distances of O^{2-} and Al^{3+} transport (nm), $B_2 = n_2 a_2$ and $B_3 = n_3 a_3$ (nm), E is the local field strength across the barrier layer (V nm^{-1}), R is the universal gas constant (8.314 J K^{-1} mol^{-1}) and T is the temperature (K). In steady state across the barrier layer $S/S_g = 2^{-1}\pi nD^2$ where n is the cell/pore surface density near Al and D is the hemispherical surface diameter across the average barrier layer unit, Fig. 3. It varies from 2.093 near the m|o interface [57] where $D = D_c$ (cell width) to $2^{-1}\pi nD_b^2$ near the o|e interface or at pore bases where D_b is the pore base diameter. The above equations describe independent transport of ions where each ionic current or transport number is univocal function of involved parameters. The independence of ions transport is strongly postulated by the considerable variability of transport numbers with conditions as shown from results found here and elsewhere [5–7, 40].

These equations resemble the high field Cabrera–Mott equation [29, 30, 51, 52] but describe oxide bulk transport processes for both cations and anions and embrace parameters like $N_{2,m}$, $N_{3,m}$, W_2', W_3', a_2 and a_3 the precise meaning of which will be given later, in subsection *The mechanism of ions transport in the barrier later*. The equations can have a physical meaning only when these parameters and possibly ν_2 and ν_3 which may vary with position across the barrier layer are univocal functions of position and possibly of local E and T. Near m|o interface where oxide density is almost constant independent of conditions and its lattice is bcc as regards the Al^{3+} sublattice [6, 7], the above parameters are constant as regards their dependence on position across the barrier layer and possibly univocal functions of local E and T. Equations (3a–4b) must apply accurately in the pure oxide sublayer near m|o interface, Table 2. For convenience, but without injuring the generality, it is assumed that the material in the barrier layer is pure oxide as in the sublayer adjacent to the m|o interface. Then the high field equations describing the ions transport in barrier layer besides Al^{3+} and O^{2-} do not involve other species like electrolyte anions, OH$^-$, etc. This approaches better reality for $H_2C_2O_4$ films incorporating the least amount of electrolyte anions among the main pore-forming electrolytes (H_2SO_4, $H_2C_2O_4$ and H_3PO_4) films [1, 31].

In the following besides the transport numbers found here those for $H_2C_2O_4$ 0.5 M and $H_2C_2O_4$ 0.5 M+Al$_3$(C$_2$O$_4$)$_3$ 0.25 M at various other conditions found earlier [5, 6, 40] were considered in order to avoid further tedious and unnecessary work. Generally, for the used transport numbers the oxalate electrolyte composition, T=0–40 °C and j=25–250 A m^{-2}, are such that as expected the real anodising temperature does not deviate notably from imposed T. This means that concurrently the concentration(s) and T are not

low and j is not high. Results were also used for H_2SO_4 1.53 M [7] at j=50–350 A m^{-2} and T=20–35 °C where film growth is regular without appearance of pitting or burning in film surface as it occurs at lower T's and higher j's [53]. At higher T's and lower j's, the oxide masses are low enough degrading the accuracy of transport numbers determination, thus such T's and j's were avoided. The transport numbers used for these electrolytes at various T's and j's are easily derived from Figs. 6 and 8 and related conditions and thus their separate citation is needless.

Analogous but simpler equations can be given for the first transient stage; formulation of such equations for the second transient stage is rather unfeasible due to the excessive change of barrier layer geometry with time. Since the transport numbers of transient stages generally do not differ noticeably from those in steady state while much more results are available for the steady state, the ensuing analysis is focused on steady state which moreover is allied with the development of characteristic channel like pores.

Application of Eqs. 4a and 4b. Determination of A_2, A_3, $-W_2'+FEB_2$ and $-W_3'+FEB_3$

Figure 6a and b present $\ln(jtn_{an})$ vs. $(RT)^{-1}$ and $\ln(jtn_{ca})=\ln[j(1-tn_{an})]$ vs. $(RT)^{-1}$ plots at j=50, 150, 250 and 350 A m^{-2} for H_2SO_4 films. Plots at j=50 and 150 A m^{-2} are given for $H_2C_2O_4$ films in Fig. 6c, d. Tolerable linear plots are observed with correlation coefficient (CORR) ≥ 0.9668, Table 3. Linearity shows that at each j the values of $\ln A_2$, $\ln A_3$, $-W_2'+FEB_2$ and $-W_3'+FEB_3$, and thus W_2', E, B_2,
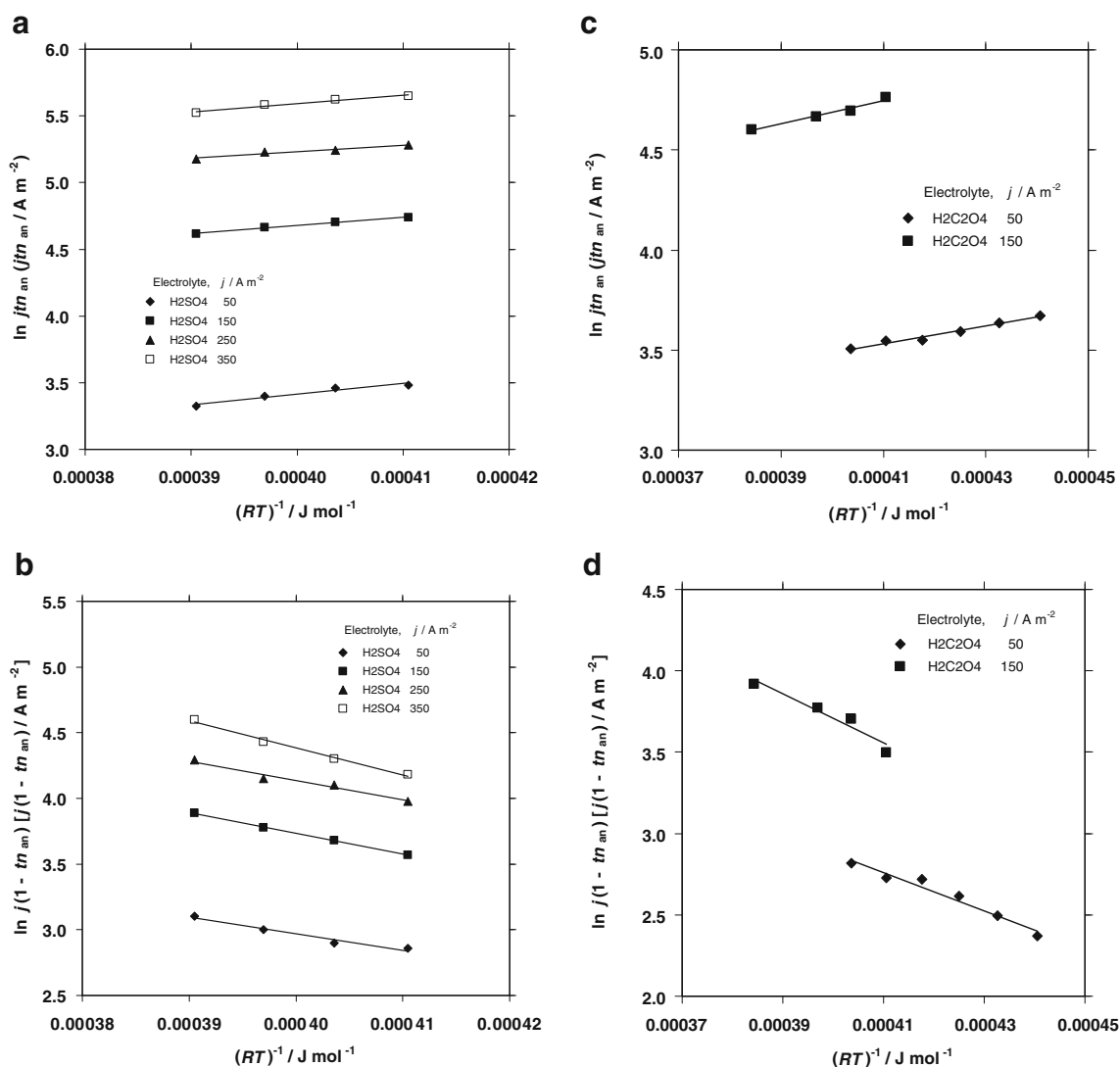

Fig. 6 Plots of $\ln(jtn_{an})$ vs. $(RT)^{-1}$ (**a, c**) and $\ln[j(1-tn_{an})]$ vs. $(RT)^{-1}$ (**b, d**) for H_2SO_4 1.53 M electrolyte films at j=50, 150, 250 and 350 A m^{-2} (**a, b**) and for $H_2C_2O_4$ 0.5 M electrolyte films at j=50 and 150 A m^{-2} (**c, d**). Data for H_2SO_4 electrolyte come from [7] and for $H_2C_2O_4$ from the present work and [5, 40]

Table 3 Values of parameters $\ln A_2$, $-W_2'+FEB_2$, $\ln A_3$ and $-W_3'+FEB_3$ derived by linear regression analysis of plots in Fig. 6

Electrolyte	j/ A m^{-2}	$\ln(A_2$/A m$^{-2})$	$-W_2'+FEB_2$/J mol^{-1}	CORR	$\ln(A_3$/A m$^{-2})$	$-W_3'+FEB_3$/J mol^{-1}	CORR
H$_2$SO$_4$ 1.53 M	50	0.154±0.154	8146.5±3850.3	0.9748	7.974±1.916	−12508.4±4785.8	0.9833
H$_2$SO$_4$ 1.53 M	150	2.210±0.440	6173.2±1097.6	0.9963	10.102±0.305	−15917.0±761.1	0.9997
H$_2$SO$_4$ 1.53 M	250	3.245±0.894	4964.3±2232.9	0.9771	10.060±2.252	−14810.7±5623.0	0.9835
H$_2$SO$_4$ 1.53 M	350	3.085±0.901	6267.7±2249.4	0.9852	12.682±1.571	−20741.4±3924.3	0.9958
H$_2$C$_2$O$_4$ 0.5 M	50	1.734±0.298	4385.9±706.6	0.9888	7.575±1.044	−11742.2±2474.2	0.9810
H$_2$C$_2$O$_4$ 0.5 M	150	2.346±0.813	5855.0±2037.0	0.9861	9.763±3.296	−15143.9±8263.1	0.9668

The confidence limit values of parameters with probability 0.95 (or uncertainty 0.05) and the correlation coefficient CORR values are also given

W_3' and B_3, are almost independent of T. The values of parameters $\ln A_2$, $\ln A_3$, $-W_2'+FEB_2$ and $-W_3'+FEB_3$ thus found are given in Table 3 where the confidence limits of their values with probability value 0.95 (or uncertainty value 0.05) are also given. It is reminded that for given v pairs of results (x_i, y_i) from which the regression analysis equation $y=a+bx$ is determined the confidence limits of a and b are given from $a \pm t_{(\alpha, (v-2))}\mathrm{Var}(a)^{1/2}$ and $b \pm t_{(\alpha, (v-2))}\mathrm{Var}(b)^{1/2}$, where $t_{(\alpha, (v-2))}$ is Student statistical distribution index corresponding to uncertainty value $\alpha=1-$probability value$=1-0.95=0.05$ and $v-2$ freedom degrees, Var$(a)=\Sigma x_i^2 S_{xy}^2/[v(\Sigma x_i^2-vx_{i,\mathrm{average}}^2)]$ and Var$(b)=S_{xy}^2/(\Sigma x_i^2-vx_{i,\mathrm{average}}^2)$ are the variances of a and b and $S_{xy}=[(v-2)^{-1}\Sigma(y_i-a-bx_i)^2]^{1/2}$ is the standard deviation of estimation.

Considering the confidence limits it is concluded that $\ln A_2$ and $\ln A_3$ certainly vary with j and this seems valid also for $-W_3'+FEB_3$ while variation or not with j of $-W_2'+FEB_2$ is unsure. The plots of $\ln A_2$ and $\ln A_3$ vs. j for H$_2$SO$_4$ electrolyte films are given in Fig. 7a and the plots of $-W_2'+FEB_2$ and $-W_3'+FEB_3$ vs. j in Fig. 7b. Since the corresponding parameters for H$_2$C$_2$O$_4$ electrolyte films do not differ strongly from those of H$_2$SO$_4$ films the results of the first were also inserted in Fig. 7a, b. The $\ln A_2$ and $\ln A_3$ show a clear tendency to increase with j, Fig. 7a, and the results of H$_2$C$_2$O$_4$ electrolyte films also advocate to this trend. Adopting roughly linear dependences of $\ln A_2$ and $\ln A_3$ on j for H$_2$SO$_4$ films the gradients of plots are 0.141 and 0.098 A^{-1} m^2 and the intercepts are 7.388 and 0.208 with CORR=0.9432 and 0.8929 showing a tolerable linearity which is however empirical probably without a definite physical meaning. The $-W_2'+FEB_2$ of H$_2$SO$_4$ films shows a slight trend to decrease with j, but considering the H$_2$C$_2$O$_4$ electrolyte results this trend further weakens by the result at the lowest j. The $-W_3'+FEB_3$ of H$_2$SO$_4$ films show a clear decline with j, Fig. 7b, and the results of H$_2$C$_2$O$_4$ electrolyte films also advocate to this trend. Roughly linear trends can be adopted for which the gradients, −6.845 and −23.593 J mol^{-1} A^{-1} m^2, and intercepts, 7,757.0 and −11,275.8 J mol^{-1}, are derived with CORR 0.6726 and 0.8781, respectively showing a moderate linearity that is empirical probably without a definite physical meaning.
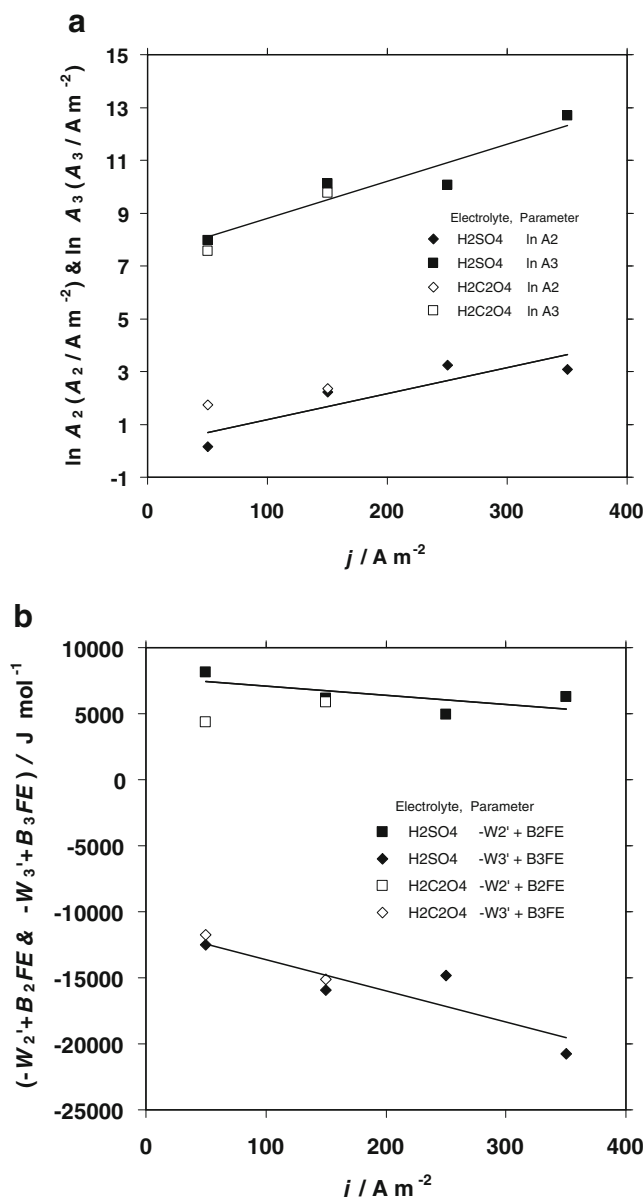

Fig. 7 Plots of $\ln A_2$ and $\ln A_3$ vs. j (**a**) and $-W_2'+FEB_2$ and $-W_3'+FEB_3$ vs. j (**b**) for H$_2$SO$_4$ 1.53 M electrolyte films. Results for H$_2$C$_2$O$_4$ 0.5 M electrolyte films were also inserted

Combination of high field equations. Determination of B_2/B_3 and a_2/a_3

After the cancellation of FE from Eqs. 4a and 4b it is inferred that

$$\ln(jtn_{an}) = (B_2/B_3)\ln[j(1-tn_{an})] + \ln A_2 - (B_2/B_3)$$
$$\times \ln A_3 + (RT)^{-1}[-W_2' + (B_2/B_3)W_3']. \quad (5)$$

The $\ln(jtn_{an})$ vs. $\ln[j(1-tn_{an})]$ plots at various j's for each T and H_2SO_4 electrolyte films are shown in Fig. 8a and for $H_2C_2O_4$ and $H_2C_2O_4+Al_2(C_2O_4)_3$ films at $T=25$ °C in Fig. 8b. Accurate straight lines are observed with CORR≥
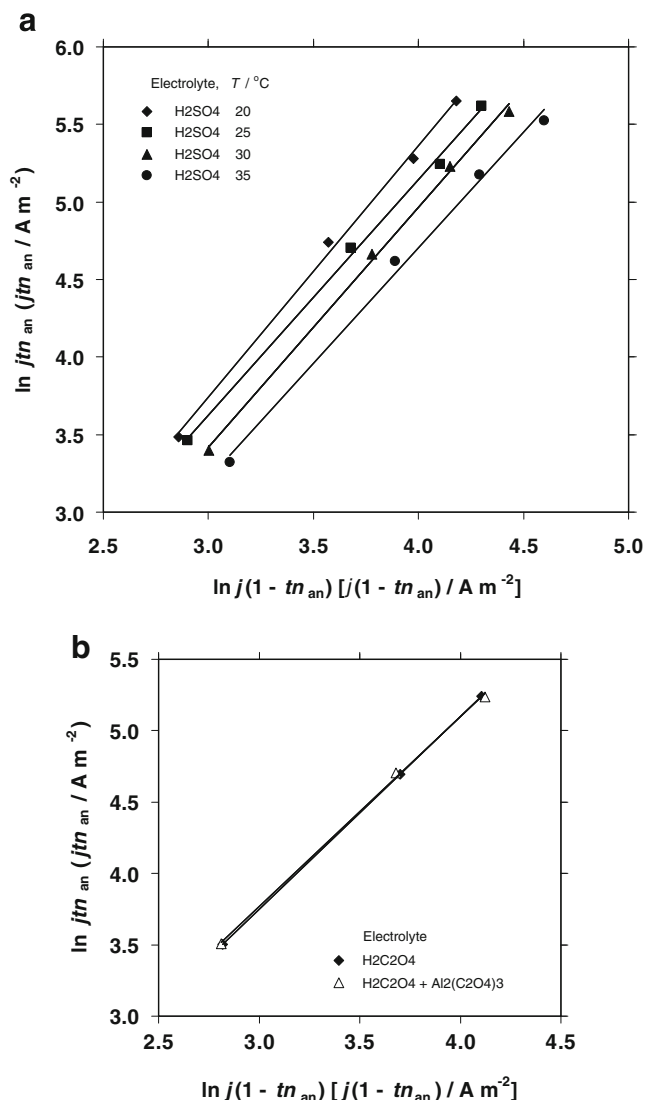

Fig. 8 Plots of $\ln(jtn_{an})$ vs. $\ln[j(1-tn_{an})]$ for H_2SO_4 1.53 M electrolyte films at $T=20$, 25, 30 and 35 °C ($j=50$, 150, 250 and 350 A m^{-2}) (a) and for $H_2C_2O_4$ 0.5 M and $H_2C_2O_4$ 0.5 M+Al$_2$(C$_2$O$_4$)$_3$ 0.25 M electrolytes films at $T=25$ °C ($j=50$, 150 and 250 A m^{-2}) (b). Data for H_2SO_4 electrolyte films come from [7], for $H_2C_2O_4$ electrolyte films from [5] and for $H_2C_2O_4+Al_2(C_2O_4)_3$ electrolyte films from [6]

0.9974 which allow the determination of parameters B_2/B_3 and $\ln A_2 - (B_2/B_3)\ln A_3 + (RT)^{-1}[-W_2' + (B_2/B_3)W_3']$ at various T's, Table 4. The confidence limits with probability 0.95 are also given. This linearity postulates that at each T the intercepts $\ln A_2 - (B_2/B_3)\ln A_3 + (RT)^{-1}[-W_2' + (B_2/B_3)W_3']$ and gradients B_2/B_3 are closely independent of j. The values of parameters for the two oxalate electrolytes films essentially coincide while considering the confidence limits these do not differ notably from those of H_2SO_4. Some small but detectable differences in transport numbers at identical j and T and derived results between oxalate and H_2SO_4 electrolytes, e.g. in Figs. 6, 7 and 8 and Tables 3 and 4, are explained mainly by that the required voltage for oxalate electrolytes at each pair of j and T is higher enough than for H_2SO_4 and especially so at lower T's and higher j's [5, 6, 40]. The real anodising temperature in the barrier layer region is slightly higher than the imposed T. Their difference is enlarged at higher j's and lower T's [32] while this difference in oxalate electrolytes must exceed appreciably that in H_2SO_4. Then the plots of oxalate electrolytes films in Fig. 8b are turned and shifted slightly to the right compared with the plots of H_2SO_4 films in Fig. 8a giving lower gradients and higher intercepts as indeed observed, Table 4. From this viewpoint the results for H_2SO_4 electrolyte films are judged more reliable.

The B_2/B_3 value shows on average a slight trend to drop with T, but considering the confidence limits it seems that B_2/B_3 is comparable for various T's allowing the adoption of a mean $B_2/B_3=1.54$ applicable for all T's. It is important to note that the mean $B_2/B_3=1.54$ is very close to $n_2a_2/n_3a_3=1.57$ when a_2 and a_3 are considered proportional to O^{2-} and Al^{3+} radii, $r_{O2-}=0.126$ nm and $r_{Al3+}=0.0535$ nm [64] respectively.

The oxide structure in the barrier layer

Before discussing details of the mechanism of ions transport in the barrier layer predicted by the results, a brief description of oxide structure in this layer is judged to be necessary in view of recently published results [6, 7]. After anodising and relaxation the oxide near m|o interface has a low density independent of conditions, 2.60 and 2.52 g cm^{-2} for oxalate and H_2SO_4 solutions [6, 7], and must be crystallised according to a bcc metastable sublattice of Al^{3+} with cell parameter 0.402 and 0.406 nm, respectively well accommodated with the fcc Al cubic lattice with parameter 0.405 nm [65]. In this structure the 6 face centre sites are occupied by O^{2-}. Each Al^{3+} at the centre of cubic cell occupies also the centre of octahedron formed by 6 nearest O^{2-}. The lattice is similar to that of perovskite (CaTiO$_3$) like structure compounds ABO$_3$ where A and B are generally different metals. Eight atoms with lower valence A occupy cube edges and an atom with higher valence B occupies its centre. Here A and B happens

Table 4 Values of parameters $\ln A_2-(B_2/B_3)\ln A_3+(RT)^{-1}[-W_2'+(B_2/B_3)W_3']$ and B_2/B_3 derived from linear regression analysis of plots in Fig. 8

Electrolyte	$T/°C$	$\ln A_2-(B_2/B_3)\ln A_3+(RT)^{-1}[-W_2'+(B_2/B_3)W_3']$	B_2/B_3	CORR
H_2SO_4 1.53 M	20	-1.118 ± 0.692	1.620 ± 0.188	0.9984
H_2SO_4 1.53 M	25	-0.932 ± 0.567	1.519 ± 0.150	0.9989
H_2SO_4 1.53 M	30	-1.218 ± 0.574	1.546 ± 0.148	0.9989
H_2SO_4 1.53 M	35	-1.255 ± 0.887	1.490 ± 0.221	0.9974
$H_2C_2O_4$ 0.5 M	25	-0.303 ± 0.007	1.350 ± 0.004	0.9999
$H_2C_2O_4$ 0.5 M+$Al_2(C_2O_4)_3$ 0.25 M	25	-0.219 ± 1.020	1.329 ± 0.285	0.9988

The confidence limit values of parameters with probability 0.95 (or uncertainty 0.05) and the correlation coefficient CORR values are also given

to be both Al atoms. As the Al metal substrate effect weakens with distance from the m|o to the o|e interface, this perovskite-like structure is gradually more and more transformed to a denser one consistent with densification of oxide to the o|e interface [6]. This denser structure must be γ or γ'-Al_2O_3 with density 3.5–3.9 g cm^{-3} [65] in agreement with that the amorphous barrier layer and pore wall oxide contains germinal γ or γ'-Al_2O_3 [29, 30, 33]. The dimensions of barrier layer and pore walls define that all lattice structures must exist as nuclei of crystals or nanocrystallites.

The γ-Al_2O_3 is considered a defect spinel structure (space group $Fd\bar{3}m$) [66] with O^{2-} in 32e Wyckoff positions which can be viewed approximately a $2\times2\times2$ array of fcc unit cells [67]. It contains vacancies in tetrahedral [68] or octahedral [69] sites rather randomly distributed from which tetrahedral sites empty in ideal spinel may be partially occupied in defect alumina structures [67, 70]. The lattice parameter of γ-Al_2O_3 is 0.79 nm [71] that is $\approx2\times0.4020$ or 2×0.4060 nm. For nanocrystalline or amorphous oxide this parameter will be on average slightly enlarged. Hence, a $2\times2\times2$ array of perovskite-like lattice unit cells is convenient to be transformed to a cell of denser nanocrystalline amorphous oxide with structure tending to resemble γ-Al_2O_3. This is supported also by that this amorphous/nanocrystalline material becomes γ-Al_2O_3 by heating at≈700 °C [34] showing affinity of their structure. The lattice cell of γ-Al_2O_3 incorporates more suitably entering and arranged atoms than a $2\times2\times2$ array of perovskite-like cells consistent with its higher density. In spinel structure the average distances of Al^{3+} and O^{2-} are smaller than in perovskite-like one thus the first structure is more stable.

The lattice of spinel ($MgO\cdot Al_2O_3$) type compounds $MO\cdot Al_2O_3$ (where M is a metal with valence 2) as already noted consists of cubic cells each of which is divided into $2\times2\times2=8$ subcells. In each subcell correspond seven atoms matching $MO\cdot Al_2O_3$. Thus each cell contains 56 ions (32 O^{2-} + 16 Al^{3+} + 8 M^{2+}). For the Al_2O_3 various limiting cases can be considered: (i$_3$) In the absence of M^{2+} and of corresponding O^{2-} the cell has a deficient structure containing 24 O^{2-} and 16 Al^{3+}; (ii$_3$) The structure is stabilised via H^+ usually embodied in Al_2O_3 structure thus each cell contains 32

O^{2-} + 16 Al^{3+} + 16 H^+; (iii$_3$) The structure is stabilised by Al^{3+} in the position of M^{2+} where each two Al^{3+} are shared in some way between three subcells, then each cell contains 32 O^{2-} + 16 Al^{3+} + 8 × (2/3) Al^{3+} or 32 O^{2-} + (64/3) Al^{3+}. A cell parameter of γ-Al_2O_3 spinel 0.79 nm [71] is adopted; strictly speaking this may change somehow from case (i$_3$) to (iii$_3$) but a common parameter is roughly adopted to obtain only an idea of oxide density and its change. The density determined from cell parameter and atoms per cell is ≈2.7, 3.2 and 4.1 g cm^{-3}, respectively for i$_3$, ii$_3$ and iii$_3$. The last value was never met experimentally in anodic alumina. The second case corresponds to hydrous oxide with contained H_2O 15% wt. But during film growth the oxide is almost anhydrous with contained $H_2O<0.5$–1% [32]. The oxide in barrier layer and pore walls of PAAF with average density 3–3.1 g cm^{-3} [72–74] experimentally found after anodising thus cannot be a γ-Al_2O_3 spinel as a whole. It must be a mixture of nuclei or nanocrystallites of perovskite-like form and some types of spinel-like forms where the portion of the first falls and of the second rises from the m|o to the o|e interface.

The spontaneous direct conversion of perovskite-like to the thermodynamically more stable spinel-like structure seems to be rather difficult under no field action due, e.g. to prohibitively high activation energies of ions diffusion in solid-state and geometrical hindrances. In steady state of film growth across the barrier layer the local E and real ionic current densities rise to the o|e interface [6]. This shows that the conversion of perovskite- to spinel-like structure and rise of spinel-like oxide portion to the o|e interface must be ascribed rather to the high field allied with ions transport and current flow. High field and related electrostriction and/or electrocompression between negatively charged o|e interface and positively charged anode [4, 29, 75] can cause momentarily local lattice transformation in the whole bulk or in certain regions of numerous nuclei or nanocrystallites of both kind structures. The transformed structure must be linked with ions transport after which the remaining transformed structure returns to ordinary one(s). The probability to return to perovskite-like structure drops from almost 1 near m|o to lower enough value near o|e

interface as the favouring effect of Al substrate weakens while that to the more stable spinel-like denser structure rises from almost 0 near m|o to high enough value near o|e interface.

The structure of relaxed after anodising oxide must be similar to that during film growth except that this transformed structure vanishes and other allied probable defects are annihilated during relaxation.

The mechanism of ions transport in the barrier layer

Self-evident would seem to describe the ions transport on the basis of their movement among neighbouring lattice cells inside the nuclei or nanocrystallites of perovskite-and/or spinel-like structure oxide and in their boundaries. But since $a_2/a_3 \approx r_{O2-}/r_{Al3+}$ the activation distances are not related actually with oxide lattice cell parameters and thus with jumps of ions from cell to cell via defects such as vacancies or interstitials voids in the aforesaid structures. This is also valid supposing that the ionic migrations are limited in the boundaries of nuclei or nanocrystallites. The ions transport mechanism must be different. Thereafter the following mechanism was conceived which concurrently assigns precise physical meaning to $N_{2,m}$, $N_{3,m}$, W_2', W_3' and $a_2/a_3 \approx r_{O2-}/r_{Al3+}$. For amorphous/nanocrystalline material the surface concentration across the barrier layer of all ions (mobile and no) of each kind can be defined considering an imaginary equipotential surface, S in Fig. 3 or S_i in Fig. 9 (where part of an O^{2-} or Al^{3+} ions cluster around S_i is also schematically depicted), normal to field strength direction. This concentration must equal the number of all ions of either kind that are sect or touched by the unit of S_i. In other words this concentration is the number, per unit surface, of ions the centres of which are included in the space between two similar surfaces S_{i-1} and S_{i+1} parallel left and right to S_i at distances equal to ionic radius. Thus for O^{2-} and Al^{3+} the distance between S_{i-1} and S_{i+1} is respectively $2r_{O2-}=$ 0.252 nm and $2r_{Al3+}=0.107$ nm. Plausibly the average jump distance is thus considered $2r_{O2-}$ and $2r_{Al3+}$ for O^{2-} and Al^{3+}. The bulk concentration (number of moles/volume) of O^{2-} and Al^{3+} is $3d(MM_{Al2O3})^{-1}$ and $2d(MM_{Al2O3})^{-1}$ where d is the local oxide density. Then the surface concentrations of all O^{2-} or Al^{3+} (number of ions/surface area) are $N_{2,m}'=2r_{O2-}\times 3d$ $(MM_{Al2O3})^{-1}N_A=6r_{O2-}d(MM_{Al2O3})^{-1}N_A$ or $N_{3,m}'=2r_{Al3+}\times 2d$ $(MM_{Al2O3})^{-1}N_A=4r_{Al3+}d(MM_{Al2O3})^{-1}N_A$, respectively. The surface concentrations of mobile ions, $N_{2,m}$ and $N_{3,m}$, are fractions of $N_{2,m}'$ and $N_{3,m}'$. The mobile ions apparently have specific geometrical positions and energies in relation to neighbouring ones and can implicitly jump the barrier of activation energy. This becomes feasible when they acquire sufficient energy. Then these ions move from an elementary volume $S_{i-1}-S_{i+1}$ to a next one, $S_{i-1}-S_{i-3}$ or $S_{i+1}-S_{i+3}$, Fig. 9, depending on the ion charge sign.
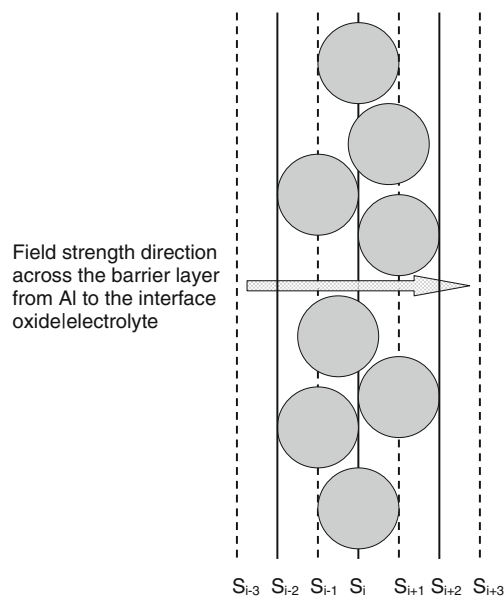

Fig. 9 Schema describing the surface concentration of O^{2-} or Al^{3+} ions in a surface S_i, across a cluster of O^{2-} or Al^{3+} ions in the barrier layer, normal to field strength direction. The ions, either O^{2-} or Al^{3+}, are in tough with S_i or are sect by S_i and thus they are confined left and right by S_{i-1} and S_{i+1} or the centres of ions lie in the space between S_{i-1} and S_{i+1}. The surface concentration of ions is thus the number of ions in a space defined by the unit surface area of S_i and thickness the diameter of ions. The surface concentration is different for these two ions. Under high field action and transformation of perovskite or spinel like lattice structure to a structure consisting of separate O^{2-} and Al^{3+} clusters in tough the ions within each cluster O^{2-} and Al^{3+} become closely packed. The transport of an ion is successful when it passes from such a space to an adjacent similar one that is from $S_{i-1}-S_{i+1}$ to $S_{i-1}-S_{i-3}$ or to $S_{i+1}-S_{i+3}$ depending on the ion charge sign

Equations 3a and 3b are of statistical physics thermodynamic nature and the exponential factor must be <1 (or the exponent must be <0) expressing the fraction of ions that have energy sufficient to jump the energy barrier. Only in this case these can describe rate-controlling steps. This is satisfied only for Al^{3+}. The transport of Al^{3+} thus seems to be the rate controlling of both ions transport. But bearing in mind the independence of Al^{3+} and O^{2-} transport this seems quite unexpected. The a_2 and a_3 are considered comparable to $r_{O2-}=0.126$ nm and $r_{Al3+}=0.0535$ nm as described above. To a first approach the region near m|o interface is examined, where oxide structure is common independent of conditions, starting from intermediate $j=150$ A m^{-2}. Local E is roughly comparable to the average E across the barrier layer ≈ 1 Vnm^{-1} [28–30] though in steady state the first is actually slightly lower than the second [6]. From $-W_2'+FEB_2=$ 6,173.2 J mol^{-1} and $-W_3'+FEB_3=-12,508.4$ J mol^{-1}, Table 3, $W_2'\approx 18,141.5$ J mol^{-1} and $W_3'\approx 27,994.5$ J mol^{-1} showing that $W_2'<W_3'$. But W_2' and W_3' are lower enough than those needed for ions diffusion in solid state under no field action ≥ 0.5–1 eV ($\geq 48{,}245$–96,490 J mol^{-1}) [76]. For E markedly lower, e.g. 0.75 Vnm^{-1} hardy met in the

literature, W_2'=12,062.8 J mol^{-1} and W_3'=24,123 J mol^{-1} which are even lower than the above while still $W_2'<W_3'$. For E markedly higher, e.g. 1.25 Vnm^{-1} also hardy met, W_2'=24,220.2 J mol^{-1} and W_3'=31,866.1 J mol^{-1} which are still low enough and $W_2'<W_3'$. The average E though varying with j is always roughly ≈1 Vnm^{-1} [12]. At the higher j=350 A m^{-2}, $-W_2'+FEB_2$=6,267.7 J mol^{-1} and $-W_3'+FEB_3$=−20,741.4 J mol^{-1} and for local E comparable to the average ≈1 Vnm^{-1} W_2'=18,047 J mol^{-1} and W_3'=36,227.6 J mol^{-1} leading to identical conclusion. This holds also for a much higher E=1.5 Vnm^{-1} hardly met giving W_2'=30,204.4 J mol^{-1} and W_3'=43,970.6 J mol^{-1}. Thus W_2' and W_3' are generally much smaller than the activation energies of ions diffusion in solid state under no field action which seems also unexpected.

The above results can be satisfactorily explained only if it is adopted that the transport of each kind ion in ordinary perovskite- or spinel-like structure lattice l_o is very difficult for reasons noted previously so that ionic current defined by j is unfeasible. Thus the transport of Al^{3+} and O^{2-} does not occur directly within l_o in a single step. It becomes feasible at proper rates after the transformation of l_o to a specific structure l_t, as shown in Fig. 10 schematically depicting also qualitatively relative changes of energies during structures transformations, as a result of high field action, emerging simultaneously in numerous positions inside the barrier layer. For convenience l_o is initially considered a single perovskite- or spinel-like oxide structure. Around an equipotential surface S across the barrier layer, Fig. 3, between the structures l_o and l_t equilibrium is established

$$l_o \leftrightarrows l_t, \tag{6}$$

where the volume of l_t is much smaller than that of l_o and thus the concentration of l_t structure ions is much smaller than that of l_o ($c_i(l_t) << c_i(l_o)$) and obey the equation $c_i(l_t)/c_i(l_o)=k_{eq}=k_0\exp(-\Delta H/RT)$ where $c_i(l_t)$ and $c_i(l_o)$ are the concentrations of l_t and l_o structures ions, k_{eq} is the equilibrium constant, $k_0=\exp(\Delta S/R)$ where ΔS is the change of entropy between l_o and l_t and ΔH is the change of enthalpy in (6) that is <0 due to the lower energy level of l_t than l_o. Then $c_i(l_t)=c_i(l_o)k_0\exp(-\Delta H/RT)$. Also $c_{O2-}(l_o)=3d(MM_{Al2O3})^{-1}$, $c_{Al3+}(l_o)=2d(MM_{Al2O3})^{-1}$ and thus $N_{2,m}=2r_{O2-}c_{O2-}(l_t)N_Af_{an}=6r_{O2-}f_{an}d(MM_{Al2O3})^{-1}N_Ak_0\exp(-\Delta H/RT)$ and $N_{3,m}=2r_{Al3+}c_{Al3+}(l_t)N_Af_{ca}=4r_{Al3+}f_{ca}d(MM_{Al2O3})^{-1}N_Ak_0\exp(-\Delta H/RT)$ where f_{an} and f_{ca} are the fractions of surface concentrations of O^{2-} and Al^{3+} in l_t that are actually mobile. Then Eqs. 3a–4b become

$$jtn_{an}S_gS^{-1} = 6r_{O2-}f_{an}k_0d(MM_{Al2O3})^{-1}$$
$$v_2n_2F\exp[(-W_2-\Delta H + n_2a_2FE)/(RT)] \tag{7a}$$

$$jtn_{ca}S_gS^{-1} = 4r_{Al3+}f_{ca}k_0d(MM_{Al2O3})^{-1}$$
$$v_3n_3F\exp[(-W_3-\Delta H + n_3a_3FE)/(RT)] \tag{7b}$$

Fig. 10 Schematic energy diagram of local transformation of original perovskite or spinel like lattice structure l_o at higher energy levels to transformed oxide structure l_t at lower energy level, $l_o \leftrightarrows l_t$. The barrier (activation) energy for the right and left direction process is generally different for the two l_o lattice structures
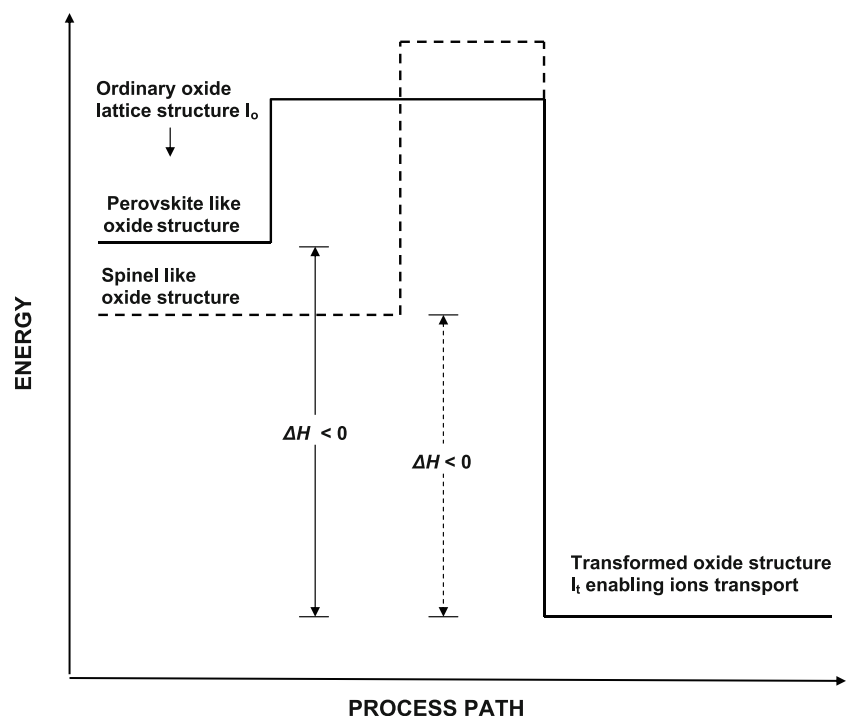
$$\ln(jtn_{an}) = \ln\left[(S/S_g)6r_{O^{2-}}f_{an}k_0 d(MM_{Al2O3})^{-1}v_2 n_2 F\right] +$$
$$(-W_2 - \Delta H + n_2 a_2 FE)/(RT) = \ln A_2 + (-W_2' + B_2 FE)/(RT)$$

(8a)

$$\ln(jtn_{ca}) = \ln\left[(S/S_g)4r_{Al^{3+}}f_{ca}k_0 d(MM_{Al2O3})^{-1}v_3 n_3 F\right] +$$
$$(-W_3 - \Delta H + n_3 a_3 FE)/(RT) = \ln A_3 + (-W_3' + B_3 FE)/(RT),$$

(8b)

where W_2 and W_3 are the real activation energies while $W_2 + \Delta H = W_2'$ and $W_3 + \Delta H = W_3'$ are the apparent ones. Then the $-W_2' + FEB_2$ and $-W_3' + FEB_3$ values, Table 3, include $-\Delta H > 0$. The W_2' and W_3' values found above are thus the apparent and not the real activation energies. The W_2 and W_3 are notably larger than these W_2' and W_3' and thus comparable to typical values of solid state ions transport. But as noted these must be lower than the very high activation energies of Al^{3+} and O^{2-} diffusion in l_o structures under no field action. The exponents not including $-\Delta H$, $-W_2 + FEB_2$ and $-W_3 + FEB_3$ are thus <0 for both ions. Hence the results are consistent with that $W_3 > W_2$, FEB_2 and FEB_3 are small compared with W_2 and W_3 and, in agreement to statistical physics thermodynamic nature of Eqs. 7a–8b, $-W_2 + FEB_2 < 0$ and $-W_3 + FEB_3 < 0$ for which $-W_2 + FEB_2 > -W_3 + FEB_3$. The ΔH is such that $-W_2 + FEB_2 > \Delta H > -W_3 + FEB_3$ giving finally $-W_2 - \Delta H + FEB_2 > 0$ and $-W_3 - \Delta H + FEB_3 < 0$ well explaining the above results. Hence the transport of each kind ion occurs in two steps, conversion of structure l_o to l_t according to (6) and the real ion transport characterised by W_2 and W_3. Since E does not vary strongly with j, Fig. 7b shows that the rise of j and attendant slight increase of E may cause an increase of W_2 and W_3 and/or of ΔH. However, its elucidation needs further extensive work exceeding the scope of study.

The f_{an} and f_{ca} could be estimated from the A_2 and A_3 values if k_0 were known which is not the case. But f_{an}/f_{ca} can be estimated from A_2/A_3 since $A_2/A_3 = (r_{O^{2-}}/r_{Al3+})(f_{an}/f_{ca})(v_2/v_3)$ where v_2 and v_3 are of the order 10^{12}–10^{13} s^{-1} [76] which can be considered roughly identical for both ions. Then $A_2/A_3 \approx (r_{O^{2-}}/r_{Al3+})(f_{an}/f_{ca})$ and from Table 1 it is found that $1.6 \times 10^{-4} \geq f_{an}/f_{ca} \geq 2.6 \times 10^{-3}$ or roughly $f_{an}/f_{ca} \approx 10^{-4}$–$10^{-3}$. Thus in the transformed structure l_t the fraction of actually mobile O^{2-} is much smaller than that of Al^{3+} by a factor $\approx 10^3$–10^4 or, from this point of view, the O^{2-} are less mobile obviously due mainly to their much larger size than that of Al^{3+}; on the other hand $W_2 < W_3$ and from this viewpoint the O^{2-} are more mobile. Their compromise yields actual mobilities of ions, described by tn_{an} and tn_{ca}, generally not differing excessively, i.e. by order(s) of magnitude.

When $j \to 0$ then $E \to 0$ and $-W_2' + FEB_2$ and $-W_3' + FEB_3$ become $-W_2'$ and $-W_3'$. Despite that W_2' and W_3' may vary with j and thus with E, a rough estimate of $-W_2'$ and $-W_3'$ at low j's can be thus made from the intercepts of plots in Fig. 7b that are 7,757 and $-11,275.8$ Jmol^{-1}. The $W_3' - W_2' = W_3 + \Delta H - (W_2 + \Delta H) = W_3 - W_2 = 19,032.8$ J mol^{-1} showing that W_3 and W_2 differ markedly while $W_3 > W_2$ verifying the above.

As expected the less stable perovskite-like structure is characterised by higher energy level than the more stable spinel-like one, Fig. 10. The structure l_t is characterised by an energy level lower than that of both structures l_o. The equilibrium (6) is feasible for both structures and thus ionic current passes via nuclei or nanocrystallites of both structures oxide after their local transformation to l_t. Because the energy levels of perovskite- and spinel-like structures are different, ΔH is expected to depend on the structure l_o transformed to l_t. Thus the average value of ΔH along an equipotential surface, Fig. 3, may increase across the barrier layer from the m|o to the o|e interface since along this direction the portion of spinel-like oxide increases and that of perovskite like decreases. The transformation each to other of spinel-like l_o to l_t is probably more difficult than that of perovskite-like l_o to l_t since the corresponding height of barrier (activation energy) in the right and possibly in the left direction is higher in the first than in the second case, Fig. 10. Besides the rise of real $j_{t,an}$ and $j_{t,ca}$ across the barrier layer, this is perhaps an additional reason why the local E rises to the o|e interface [6]. This rise may be necessary for the transformation of l_o (changing on average along this direction in favour of spinel-like structure) to l_t for establishing constant ionic current across this layer.

Since the process (6) concerns both perovskite- and spinel-like structures, irrespective of l_o the left direction process can give either perovskite- or spinel-like structure. The probability of reappearance of each structure l_o depends on the distance from Al substrate that favours perovskite-like structure and on the average environment of l_o where local transformation to l_t occurred that acts as matrix and which changes in favour of spinel-like structure to the o|e interface. The l_t is thus involved also in the conversion of perovskite-like to more stable spinel-like structure at portion rising to the o|e interface.

The l_t structure must be extraordinary. Under high field action allied with electrostriction and/or electrocompression between negatively charged interface and positively charged anode [4, 29, 75], the l_t at a position is most probably a pair of clusters consisting of solely Al^{3+} and O^{2-} in touch. Each cluster embraces a little number of closely packed planar ionic layers which are dense but include vacancies. This clusters structure probably reduces the total void space of ordinary structures l_o. Figure 9 gives an idea of a cluster if Al^{3+} or O^{2-} ions are densely packed, e.g. in layers $S_{i-2} - S_i$

and $S_i - S_{i+2}$, a few such layers are repeated and ions vacancies exist in cluster bulk. Such structure must be at lower energy level while vacancies in each Al^{3+} or O^{2-} cluster provide average half jump (activation) distances comparable to ions radii within clusters and up to their boundaries where the moved ions are assimilated by adjacent ordinary structure. After ions transport the residual l_t returns to l_o structure(s) while l_t emerges at other position(s). Only thus moved ions produce ionic current. The conversion $l_o \rightarrow l_t \rightarrow l_o$ without such ionic movement(s) does not produce ionic current. Clusters thus play an important role in the mechanism of recrystallisation and densification of oxide to the o|e interface predicted by the relevant film growth model [40]. These can also play a similar role in the flow of material predicted from the relevant film growth model [4, 39], acting as lubricant for sliding shift, under above stresses, of nuclei or nanocrystallites or of their groups enclosed in a network of continuously formed and deformed l_t structure positions.

The transport of each kind ion in corresponding clusters described by its own Eq. 8a or 8b and parameters W_2, a_2, f_{an} etc. or W_3, a_3, f_{ca} etc. is consistent with the noted independence of ions transport. The only condition among jtn_{an} and jtn_{ca} is that their sum must equal the imposed constant j. This is achieved by power supplier imposing proper variable voltage and thus potential drop in the barrier layer or proper local and average E. The E defines directly ionic currents and may affect certain parameters of equations which in turn also affect these currents. Equations 8a and 8b show that the rise of A_2 and A_3 with j, Fig. 7a, is due mostly to a rise of f_{an} and f_{ca} which are expected to vary appreciably with E. The A_2 and A_3 may be secondarily affected by change of ν_2 and ν_3 that may vary less with E. Since these equations describe ions transport at each equipotential surface in barrier layer, A_2 and A_3 also characterise each such surface. The slight increase of d to the o|e interface must exert a tiny effect counterbalanced by the reduction of S/S_g and proper changes of f_{an} and f_{ca} and/or ν_2 and ν_3.

Inherent uncertainties in determining accurate activation energies

The above analysis was partly based on the evaluation and treatment of activation energies, e.g. W_2' and W_3'. Their accurate determination, variation across the barrier layer and relation anticipates the knowledge at various conditions of the accurate local E and its distribution across this layer. The latter demands the accurate determination of potential drop and its distribution across the barrier layer which is experimentally unfeasible. Even in the simplest case of the accurate determination of average E, it demands the precise experimental determination of barrier layer thickness, which is not always possible for various reasons, and of potential

drop across this layer which is unfeasible. The latter is roughly approximated by the anodising voltage and in the best case more accurately by P_{an} (vs. SHE or other reference electrode). During anodising the thickness of barrier layer may also differ from that after anodising and oxide relaxation, due e.g. to some shrinkage resulting from its electrostriction or electrocompression under high field action or to oxide density distribution across the layer not coinciding with that after anodising. Thus the real average E during anodising may differ from that found by potential drop evaluated during anodising and barrier layer thickness found after anodising and oxide relaxation.

Even if the thickness of barrier layer is considered precisely known, the calculated average E and related W_2' and W_3' embody inherent uncertainties as depending to some extent on the assigned potential drop in this layer. At corresponding conditions the anodising voltage and P_{an} are higher enough in oxalate electrolytes than in H_2SO_4 and their relative % deviation from the real potential drop must be lesser in oxalate electrolytes. Therefore the average E determined by anodising voltage or P_{an} is expected to approach better reality in oxalate electrolytes. But, as previously noted the deviation of real anodising temperature from imposed T affecting the results is larger in oxalate electrolytes. Thus uncertainties in determining the accurate average E always intrude and W_2' and W_3' can be calculated only approximately. Despite these uncertainties literature data [9, 12, 29, 30] show that always the average E does not differ markedly from roughly 1 V nm^{-1} while the local E must vary relatively slightly inside barrier layer [6] thus the calculated values of W_2' and W_3' are tolerable and the relevant analysis is reliable. Further uncertainties intrude in determining the accurate W_2 and W_3 as the presently unknown ΔH may vary across the barrier layer and with conditions.

The calculation of accurate activation energies depends also on the knowledge of accurate a_2 and a_3 values. Since a_2/a_3 was found almost independent of conditions, implying that a_2 and a_3 are similarly almost independent, and a_2 and a_3 are proportional to ions radii, the only conceivable relation of activation distances with these radii is that described in the disclosed ions transport mechanism. For this reason any uncertainty concerning the used a_2 and a_3 values is unimportant also advocating to the reliability of previous analysis.

From the above it seems that even when the charge transport equations apply precisely the determination of activation energies with high accuracy is unfeasible, thus their values can be only approximated.

Conclusions

1. Al anodising at low temperatures 0 and 5 °C in oxalic acid electrolyte showed that the efficiency for Al

consumption is close to that anticipated by Faraday's law while the efficiency of oxygen evolution, visually detected at these temperatures, is negligible. Also the oxide production efficiency near m|o interface and the O^{2-} transport number increase with current density, decrease with temperature and are almost independent of electrolyte concentration.

2. High field electrochemical kinetic equations embodying ions transport numbers and describing independent Al^{3+} and O^{2-} transport across the barrier layer were suitably formulated. Their application in oxalate and sulphuric acid electrolytes films enabled penetration to the actual Al^{3+} and O^{2-} transport mechanism.

3. The average half jump activation distances of Al^{3+} and O^{2-} transport inside the barrier layer are closely independent of conditions and proportional, most likely comparable, to ions radii.

4. The real activation energy of Al^{3+} transport is larger than that of O^{2-}, e.g. by ≈ 19 kJ mol^{-1} at low current densities, but the fraction of actually mobile Al^{3+} is $\approx 10^3$–10^4 times larger than that of O^{2-}. These explain why the Al^{3+} and O^{2-} transport numbers generally do not differ excessively, i.e. by order(s) of magnitude.

5. The transport of both ions must take place via two steps. The first is an equilibrium process that anticipates conversion of parts or of the whole bulk of nuclei or nanocrystallites of ordinary perovskite- or spinel-like structure oxide, hardly allowing ions transport, to a transformed structure emerging at numerous positions dispersed in barrier layer. It consists likely of Al^{3+} and O^{2-} clusters which enable ions transport. The second, rate-controlling step, is the real ion transport process within clusters occurring independently for each ion and characterised by its own kinetic parameters. Then the transformed structure returns to ordinary one(s).

6. The peculiar structure consisting of clusters predicted by the present study which allows transport of ions via the disclosed mechanism is important as serving for an in depth comprehension of the mechanism of oxide production and film growth and thus exciting for further investigation of its nature.

References

1. Thompson GE (1997) Thin Solid Films 267:192–201
2. Brown F, Mackintosh WD (1973) J Electrochem Soc 120:1096–1102
3. Thompson GE, Xu Y, Skeldon P, Shimizu K, Han SH, Wood GC (1987) Phil Mag B 55:651–667
4. Garcia-Vergara SJ, Skeldon P, Thompson GE, Habazaki H (2006) Electrochim Acta 52:681–687
5. Patermarakis G, Chandrinos J, Masavetas K (2007) J Solid State Electrochem 11:1191–1204
6. Patermarakis G, Karayianni H, Masavetas K, Chandrinos J (2009) J Solid State Electrochem 13:1831–1847
7. Patermarakis G, Moussoutzanis K (2009) Electrochim Acta 54:2434–2443
8. Zhou F, Mohamed Al-Zenati AK, Baron-Wiecheć A, Curioni M, Garcia-Vergara SJ, Habazaki H, Skeldon P, Thompson GE (2011) J Electrochem Soc 158:C202–C214
9. Sheasby PG, Pinner R (2001) The surface treatment and finishing of aluminium and its alloys, 6th edn. ASM International and Finishing Publications Ltd, USA
10. Martin CR (1996) Chem Mater 8:1739–1746
11. Kovtyukhova N, Mallouk TE (2005) Adv Mater 17:187–192
12. Sulka GD (2008) Highly ordered anodic porous alumina formation by self-organized anodizing. In: Eftekhari A (ed) Nanostructured materials in electrochemistry. Wiley-VGH, Wienheim
13. Ganley JC, Riechmann KL, Seebauer EG, Masel RI (2004) J Catal 227(1):26–32
14. Pellin MJ, Stair PC, Xiong G, Elam JW, Birrell J, Curtiss L, George SM, Han CY, Iton L, Kung H, Kung M, Wang HH (2005) Catal Lett 102(3–4):127–130
15. Surganov VF, Gorokh GG (1993) Mater Lett 17:121–124
16. Surganov V, Janson C, Nielsen JCG, Morgen P, Gorokh G, Larsen AN (1988) Electrochim Acta 33:517–519
17. Dell'Oca CJ, Fleming PJ (1976) J Electrochem Soc 123:1487–1493
18. Parkhutik VP (1986) Corros Sci 26:295–310
19. Parkhutik VP, Shershulsky VI (1992) J Phys D Appl 25:1258–1263
20. Jessensky O, Müller F, Gösele U (1998) Appl Phys Lett 72(10):1173–1175
21. Zhang L, Cho HS, Li F, Metzger RM, Doyle WD (1998) J Mater Sci Lett 17:291–294
22. Jessensky O, Müller F, Gösele U (1998) J Electrochem Soc 145:3735–3740
23. Nielsch K, Choi J, Schwirn K, Wehrspoh RB, Gösele U (2002) Nano Lett 2(7):677–680
24. Li AP, Müller F, Birner A, Nielsch K, Gösele U (1997) J Appl Phys 84(11):6023–6026
25. Li AP, Müller F, Gösele U (2000) Electrochem Solid State Lett 3(3):131–134
26. Masuda H, Yotsuy M, Asano M, Nishio K, Nakao M, Yokoo A, Tamamura T (2001) Appl Phys Lett 78(6):826–828
27. Pan H, Lin J, Feng Y, Gao H (2005) IEEE Transac Nanotechnol 3:462–467
28. Keller F, Hunter MS, Robinson DL (1953) J Electrochem Soc 100:411–419
29. Diggle JW, Downie TC, Goulding CW (1969) Chem Rev 69:365–405
30. Young L (1961) Anodic oxide films. Academic, London
31. Thompson GE, Furneaux RC, Wood GC (1978) Corros Sci 18:481–498
32. Patermarakis G, Lenas P, Karavassilis C, Papayiannis G (1991) Electrochim Acta 36:709–725
33. Patermarakis G, Kerassovitou P (1992) Electrochim Acta 37:125–137
34. Ruckenstein E, Chu YF (1979) J Catal 59:109–122
35. O'Sullivan JP, Wood GC (1970) Proc R Soc Lond A 317:511–543
36. Li F, Zhang L, Metzger RM (1998) Chem Mater 10:2470–2480
37. Zhu XF, Li DD, Song Y, Xiao YH (2005) Mater Lett 59:3160–3163
38. Zhu X, Liu L, Song Y, Jia H, Yu H, Xiao X, Yang X (2008) Mater Lett 62:4038–4040
39. Garcia-Vergara SJ, Skeldon P, Thompson GE, Hashimoto T, Habazaki H (2007) J Electrochem Soc 154:C540–C545
40. Patermarakis G (2009) J Electroanal Chem 635:39–50
41. Napolskii KS, Roslyakov IV, Eliseev AA, Petukhov AV, Byelov DV, Grigiryeva NA, Bouwman WG, Lukashin AV, Kvashnina KO, Chumacov AP, Grigoryev SV (2010) Appl Crystallogr 43:531–538

42. Masuda H, Asoh H, Wanatab M, Nishio M, Nakao M, Tamamura T (2001) Adv Mater 13:189–192
43. Kustandi TS, Loh WW, Gao H, Low HY (2010) ACS Nano 4 (5):2561–2568
44. Masuda H, Fukuda K (1995) Science 268:1466–1468
45. Sulka GD, Stroobants S, Moshehalkov V, Borghs G, Celis JP (2002) J Electrochem Soc 149(7):D97–D103
46. Masuda H, Hasegwa F, Ono S (1997) J Electrochem Soc 144:L127–L130
47. Montero-Moreno JM, Sarret M, Müller C (2010) Micropor Mesopor Mat 136:68–74
48. Cherki C, Siejka J (1973) J Electrochem Soc 120:784–791
49. Davies JA, Domeij B, Pringle JPS, Brown F (1965) J Electrochem Soc 112:675–680
50. Davies JA, Domeij B (1963) J Electrochem Soc 110:849–852
51. Cabrera N, Mott NF (1949) Rep Prog Phys 12:163–184
52. Dignam MJ, Taylor DF (1970) Cand J Chem 49:416–424
53. Patermarakis G, Moussoutzanis K (2001) Corros Sci 43:1433–1464
54. Wood GC, O'Sullivan JP (1970) Electrochim Acta 15:1865–1876
55. Patermarakis G, Moussoutzanis K (2011) J Electroanal Chem 659:176–190
56. Patermarakis G, Moussoutzanis K, Chandrinos J (2001) J Solid State Electrochem 6:39–54
57. Patermarakis G, Moussoutzanis K (1995) Electrochim Acta 40:699–708
58. Houser JE, Heber KR (2006) J Electrochem Soc 153:B566–B573
59. Wu Z, Richter C, Menon L (2007) J Electrochem Soc 154(1):E8–E12
60. Vogel AI (1976) Macro and semimicro quantitative analysis. Longman, London
61. Alexeyev VN (1980) Qualitative chemical analysis. Mir, Moscow
62. Siejka J, Ortega C (1977) J Electrochem Soc 124:883–891
63. Belca I, Kasalica B, Zekovic LJ, Jovanic B, Vasilic R (1999) Electrochim Acta 45:993–996
64. "Oxygen." Chemicool Periodic Table. Chemicool.com. 13 Jun. 2011. Web. 12/10/2011 <http://www.chemicool.com/elements/oxygen.html>., "Aluminum." Chemicool Periodic Table. Chemicool.com. 9 May 2011. Web. 12/10/2011 <http://www.chemicool.com/elements/aluminum.html>
65. Weast RC (ed) (1980) Handbook of chemistry and physics, 60th edn. CRC, Boca Raton
66. Lippens BC, De Boer JH (1964) Acta Crystallogr 17:1312–1321
67. Hahn T (1995) International tables of crystallography, vol. A. Kluwer Academic Publishers, London
68. Mo SD, Xu YN, Ching WY (1997) J Amer Cer Soc 80:1193–1197
69. McHale JM, Navrotsky A, Perrota AJ (1997) J Phys Chem B 101:603–613
70. Zhou RS, Snyder RL (1991) Acta Crystallogr B 47:617–630
71. Samsonov GV (1973) The oxide handbook. IFI/Plenum, New York
72. Skeldon P, Shimizu K, Thompson GE, Wood GC (1983) Surf Interface Anal 5:247–251
73. Lohrengel MM (1993) Mater Sci Eng R 11:243–294
74. Lee S, White HS (2004) J Electrochem Soc 151(8):B479–B483
75. Bradhurst DH, Leach JSL (1966) J Electrochem Soc 113:1245–1249
76. Kittel C (1968) Introduction to solid state physics, 3rd edn. Wiley, New York